



HAL
open science

A comparison of refinement indicators for the p-adaptive simulation of steady and unsteady flows with discontinuous Galerkin methods

Fabio Naddei, Marta de La Llave Plata, Vincent Couaillier, Frédéric Coquel

► To cite this version:

Fabio Naddei, Marta de La Llave Plata, Vincent Couaillier, Frédéric Coquel. A comparison of refinement indicators for the p-adaptive simulation of steady and unsteady flows with discontinuous Galerkin methods. 2018. hal-01787788

HAL Id: hal-01787788

<https://hal.science/hal-01787788>

Preprint submitted on 7 May 2018

HAL is a multi-disciplinary open access archive for the deposit and dissemination of scientific research documents, whether they are published or not. The documents may come from teaching and research institutions in France or abroad, or from public or private research centers.

L'archive ouverte pluridisciplinaire **HAL**, est destinée au dépôt et à la diffusion de documents scientifiques de niveau recherche, publiés ou non, émanant des établissements d'enseignement et de recherche français ou étrangers, des laboratoires publics ou privés.

A comparison of refinement indicators for the p -adaptive simulation of steady and unsteady flows with discontinuous Galerkin methods

Fabio Naddei^a, Marta de la Llave Plata^a, Vincent Couaillier^a, Frédéric Coquel^b

^aONERA - The French Aerospace Lab, FR-92320 Châtillon, France

^bÉcole Polytechnique, FR-91128 Palaiseau, France

Abstract

This paper presents an analysis of refinement indicators for the simulation of steady and unsteady flows by means of p -adaptive algorithms for discontinuous Galerkin (DG) methods. Residual-error, discretization-error and feature-based indicators are compared by studying their effect on convergence history, computational gain and refinement regions selected by the adaptive algorithm. The analysis is initially carried out on steady flow configurations. Static p -adaptive simulations of the periodic flow past a cylinder at $Re = 100$ are then performed. Compared to uniform p -refinement, a reduction between 50% and 75% in the number of degrees of freedom is obtained for all test cases considered. The accuracy and efficiency observed for the VMS [1] and spectral decay [2] indicators demonstrate their great potential for the adaptive simulation of unsteady flows.

Keywords: error-based adaptation; high-order discontinuous Galerkin; *a posteriori* error estimation; p -refinement; discretization error estimation; residual error estimation;

1. Introduction

Discontinuous Galerkin (DG) methods [3, 4, 5, 6] are a class of high-order methods based on the variational projection of the Navier-Stokes equations and combine features of Finite Volume (FV) and Finite Element (FE) methods. One remarkable property of this method is the possibility of largely reducing the computational cost of the simulations by increasing the local spatial resolution by either locally reducing the mesh size (h -refinement), or by locally increasing the polynomial order of the approximation within the elements (p -refinement). Local p -refinement can reduce dissipation and dispersion errors in regions where the solution is smooth thus allowing for the accurate resolution of unsteady turbulent phenomena with a lower number of degrees of freedom (DOFs) as compared to Finite Difference (FD) and FV methods [7, 8]. In addition, h -refinement can be employed in combination with p -refinement to isolate regions characterized by geometrical and physical discontinuities.

hp -adaptive techniques are based on the definition of a refinement indicator and an hp -decision algorithm. Refinement indicators, usually relying on *a posteriori* error estimates, identify regions

URL: fabio.naddei@onera.fr (Fabio Naddei)

where an increased spatial resolution is required. The *hp*-decision procedure, often based on the evaluation of the smoothness of the solution, selects the refinement strategy (*h* or *p*) to be adopted.

Considerable efforts have been dedicated to the development of robust *a posteriori* error estimators for partial differential equations. We refer to the works by Roy [9], Houston and Süli [10], and Mitchell and McClain [11], for a review of error estimation strategies and their use for *hp*-adaptive algorithms.

The selection of the most appropriate refinement indicator for an adaptive procedure is the result of a compromise between the computational overhead due to the evaluation of the error estimator, the desired level of accuracy of the adapted solution and the robustness of the refinement indicator. This is of particular interest for the development of adaptive algorithms for turbulent flow simulations because of the high computational cost required for this type of applications. However, a fair analysis of different refinement indicators is an arduous task. This is the consequence of the lack of a systematic comparison using the same configuration and numerical scheme, as well as the fact that the same refinement indicator can be open to multiple interpretations.

The goal of this work is thus to provide such an analysis with the specific objective of identifying advantages and drawbacks in the development of adaptive algorithms for the simulation of unsteady flows by means of DG methods. The focus of this research is on the analysis of *p*-refinement algorithms, the extension of these results to *h*- or *hp*-adaptive algorithms is the subject of future research.

The large variety of refinement indicators reported in the literature can be classified in three main groups:

- (i) *Feature based indicators* are often derived from physical or theoretical properties of the problem to be solved or from the observation that some phenomena must be fully resolved in order to obtain an accurate representation of the flow field. Examples include methods for vortex detection [12], boundary layer detection, or interface detection for two-phase flows [13]. These methods are often inefficient, lack of robustness and do not take into account error propagation. However, they are often inexpensive, simple to implement and can provide reasonably good results when employed by expert users.
- (ii) *Discretization-Error (DE) based indicators* identify for refinement regions characterized by high values of the error between the numerical and the exact solution. The most common strategy to estimate DE is to perform two simulations on successively refined discretization spaces and compare the two numerical solutions [14]. Other possible approaches include the computation of estimates of higher-order solutions [15], estimates of truncation error through the decay rate of Legendre expansion coefficients [16] or the exploitation of superconvergent phenomena [17]. A possible drawback is that the DE is produced in regions of insufficient spatial resolution and then diffused and convected as a scalar quantity [9, 18]. An adaptation process which is driven by local values of DE would thus also refine regions where the error is transported and not produced thus exhibiting sub-optimal performance. For this reason, Residual-Error (RE) based and τ -based (TE) methods are often employed in the FE and FV frameworks respectively. This is justified by the fact that the TE and the RE appear as production terms in the discretization error transport equations [9, 18, 19, 20, 21]. In the FE framework RE-based methods can often be classified as DE-based estimator since RE estimates can provide DE bounds provided that suitable norms are employed.

(iii) *Goal oriented indicators* evaluate the contribution of the numerical error to the error in the evaluation of a target functional (e.g. the drag or the lift coefficient). Their derivation requires the computation of element-wise residuals which are weighted by the solution of a dual problem derived from the discretization employed and the target quantity. These methods capture the inherent mechanism of error propagation in hyperbolic and nearly-hyperbolic problems. Thanks to this property, they have been shown to provide the lowest computational cost to achieve a prescribed level of accuracy when a target functional is the goal of a simulation [21, 22, 23, 24]. The solution of the adjoint problem must be performed in a refined discretization space [22] and requires the backward integration in time for unsteady problems, thus requiring the numerical solution to be known at each previous time step.

In this work, we focus our analysis on DE- and RE-based refinement indicators. Goal oriented/adjoint-based methods are not considered here. Despite the fact that a vast number of authors have demonstrated their superiority with respect to DE methods for steady problems, their high memory requirements and high computational cost prohibit their application to turbulent flow configurations of industrial interest. Conversely, DE- and feature-based refinement indicators have already been successfully applied to LES and are of interest thanks to the very limited computational overhead required [12, 25, 26, 27].

The analysis proposed in this work targets the research of possible advantages or drawbacks of different DE and RE error estimators for p -adaptive simulations of steady and unsteady flows. For this purpose, we study the effect of different indicators on the convergence history of the adaptive procedure, the computational gain provided and the spatial regions selected for refinement. We do not compare the efficiency of different refinement indicators on estimating the error of the numerical solution as different indicators measure different errors or employ different norms.

This paper is organised as follows. In section 2 the governing equations and the DG method are briefly introduced. In section 3 a brief review of the considered refinement indicators is presented along with their relationship with other refinement indicators employed in the literature. In section 4 the direct comparison of refinement indicators on inviscid and viscous steady and unsteady flows is provided. A comparison in terms of potential implementation issues and computational cost is reported in section 5. The main conclusions from this research are presented in section 6.

2. Model problem and discretization

The simulations presented in this work have been performed using the DG unstructured solver *Aghora* developed at ONERA [28] solving the compressible Navier-Stokes equations. The physical model and the DG method used in this work are recalled in this section.

2.1. Physical model

Let $\Omega \in \mathbb{R}^d$ be a bounded domain, where d is the space dimension, the compressible Navier-Stokes equations take the form :

$$\partial_t \mathbf{u} + \nabla \cdot \mathcal{F}_c(\mathbf{u}) - \nabla \cdot \mathcal{F}_v(\mathbf{u}, \nabla \mathbf{u}) = 0 \quad (1)$$

with associated initial conditions $\mathbf{u}(\cdot, 0) = \mathbf{u}_0(\cdot)$ and appropriate boundary conditions prescribed on $\partial\Omega$. The vector $\mathbf{u} = (\rho, \rho\mathbf{v}, \rho E)^T$ represents the conservative state variables, with ρ being the

density, $\mathbf{v} = (U_1, U_2, U_3)^T$ the velocity vector and $E = \frac{p}{(\gamma-1)\rho} + \frac{\mathbf{v}\cdot\mathbf{v}}{2}$ the specific total energy. Here, p is the static pressure and $\gamma = \frac{C_p}{C_v} > 1$ the ratio of specific heats. The nonlinear convective and diffusive fluxes in Eq. (1) are defined respectively as:

$$\mathcal{F}_{c,i}(\mathbf{u}) = \begin{bmatrix} \rho U_i \\ \rho U_1 U_i + p \delta_{i1} \\ \rho U_2 U_i + p \delta_{i2} \\ \rho U_3 U_i + p \delta_{i3} \\ \rho U_i E \end{bmatrix} \quad \mathcal{F}_{v,i}(\mathbf{u}, \nabla \mathbf{u}) = \begin{bmatrix} 0 \\ \tau_{i1} \\ \tau_{i2} \\ \tau_{i3} \\ \tau_{ik} U_k - q_i \end{bmatrix} \quad (2)$$

with

$$\tau_{ij} = \mu \left(\frac{\partial U_j}{\partial x_i} + \frac{\partial U_i}{\partial x_j} - \frac{2}{3} \frac{\partial U_k}{\partial x_k} \delta_{ij} \right) \quad (3)$$

$$q_i = -\lambda \frac{\partial T}{\partial x_i} \quad (4)$$

where μ is the dynamic viscosity, described by the Sutherland law, T denotes the temperature, related to the pressure and density by the equation of state, $\lambda = \mu \frac{C_p}{Pr}$ is the thermal conductivity and Pr refers to the Prandtl number.

2.2. The DG method

The domain Ω is partitioned in a shape-regular mesh \mathcal{T}_K consisting of N non-overlapping and non-empty elements K of characteristic size h_K . We also define the sets \mathcal{E}_i and \mathcal{E}_b of interior and boundary faces in \mathcal{T}_K such that $\mathcal{E}_h = \mathcal{E}_i \cup \mathcal{E}_b$.

Let $S_h^p = \{\phi \in L^2(\Omega) : \phi|_K \in \mathcal{P}^p(K), \forall K \in \mathcal{T}_K\}$ be the functional space formed by piecewise polynomials of either total or partial degree at most p defined in the element, and $(\phi_K^1, \dots, \phi_K^{N_p}) \in \mathcal{P}^p(K)$ a hierarchical and orthonormal basis of $\mathcal{P}^p(K)$ of dimension $N_p = (p+1)^d$. The polynomial degree p will in general depend on the element and will be indicated as p_K when necessary. For the DG method used in this research, the orthonormal basis is obtained by applying a modified Gram-Schmidt procedure to a tensor product of monomials of degree at most p . This produces a diagonal mass matrix even on curved elements [29]. The solution in each element is thus expressed as

$$\mathbf{u}_h(\mathbf{x}, t) = \sum_{l=1}^{N_p} \phi_K^l(\mathbf{x}) \mathbf{u}_K^l(t), \quad \forall \mathbf{x} \in K, K \in \mathcal{T}_K, \forall t > 0 \quad (5)$$

in which the polynomial coefficients $(\mathbf{u}_K^l)_{1 \leq l \leq N_p}$ represent the DOFs of the discrete problem in element K . The semi-discrete variational form of Eq. (1) therefore reads: find \mathbf{u}_h in S_h^p such that $\forall \phi_h \in S_h^p$

$$\int_{\mathcal{T}_K} \phi_h \partial_t \mathbf{u}_h dV + \mathcal{L}_c(\mathbf{u}_h, \phi_h) + \mathcal{L}_v(\mathbf{u}_h, \phi_h) = 0 \quad (6)$$

In Eq. (6) \mathcal{L}_c and \mathcal{L}_v represent the variational projection of the convective and viscous terms onto the functional space S_h^p . For a given interface e in \mathcal{E}_i we define u^+ and u^- the value of a

variable at both sides of the element faces, the average operator $\{\{u\}\} = (u^+ + u^-) / 2$ and the jump operator $[[u]] = u^+ - u^-$. The DG discretization of the convective terms then reads

$$\mathcal{L}_c(\mathbf{u}_h, \phi_h) = - \int_{\mathcal{T}_K} \mathcal{F}_c(\mathbf{u}_h) \cdot \nabla_h \phi_h dV + \int_{\mathcal{E}_i} [[\phi_h]] H_c(\mathbf{u}_h^+, \mathbf{u}_h^-, \mathbf{n}) dS + \int_{\mathcal{E}_b} \phi_h^+ \mathcal{F}_c(\mathbf{u}_b) \cdot \mathbf{n} dS \quad (7)$$

The boundary values $\mathbf{u}_b = \mathbf{u}_b(\mathbf{u}_h^+, \mathbf{u}_{\text{ext}}, \mathbf{n})$, with \mathbf{u}_{ext} a reference external state, are computed in order to impose the appropriate boundary condition on each boundary \mathcal{E}_b .

The function H_c in Eq. (7) is a numerical flux that approximates the convective flux on an element face and must be chosen to be conservative and consistent. In the simulations presented in this work the local Lax-Friedrichs (LLF) flux has been employed.

For the discretization of the viscous terms in Eq. (6) the BR2 method of Bassi and coworkers [30, 31] has been employed, namely:

$$\begin{aligned} \mathcal{L}_v(\mathbf{u}_h, \phi_h) = & \int_{\mathcal{T}_K} \mathcal{F}_v(\mathbf{u}_h, \nabla_h \mathbf{u}_h + \mathbf{L}_h) \cdot \nabla \phi_h dV - \int_{\mathcal{E}_i} [[\phi_h]] \{\{\mathcal{F}_v(\mathbf{u}_h, \nabla_h \mathbf{u}_h + \eta_e \mathbf{I}_h^e)\}\} \cdot \mathbf{n} dS \\ & - \int_{\mathcal{E}_b} \phi_h^+ \mathcal{F}_v(\mathbf{u}_b, \nabla \mathbf{u}_b + \eta_e \mathbf{I}_h^e) \cdot \mathbf{n} dS \end{aligned} \quad (8)$$

where η_e is a numerical parameter that ensures the stability of the method. The global lifting operator \mathbf{L}_h is defined as the sum of the local lifting operators \mathbf{I}_h^e : $\mathbf{L}_h = \sum_{e \in \partial K} \mathbf{I}_h^e$ where \mathbf{I}_h^e has support on the elements adjacent to $e \in \mathcal{E}_i$ and is obtained from the solution of the following problem on the internal faces:

$$\int_{K^+ \cup K^-} \phi_h \mathbf{I}_h^e dV = - \int_e \{\{\phi_h\}\} [[\mathbf{u}_h]] dS \quad \forall \phi_h \in S_h^p \quad (9)$$

A similar expression for the local lifting coefficients, consistent with the boundary conditions, is obtained on \mathcal{E}_b .

The semi-discrete equation Eq. (6) is discretized in time by means of a time integration scheme. In this work all steady solutions are obtained by employing an implicit backward-Euler scheme relying on the GMRES method and ILU(0) preconditioning for the solution of the corresponding linear system. The last unsteady test case considered is solved via an explicit second order Runge-Kutta Heun scheme.

The integrals in Eq. (6) are computed by means of the Gauss-Legendre quadrature with $q = p + 1 + m$ points in each space direction, where m denotes the number of overintegration points used for dealiasing purposes.

3. Refinement and marking procedure

An adaptive p -refinement algorithm defines locally the polynomial degree p_K used to approximate the solution within a given element. In the case of p -adaptive simulations of steady flows the refinement procedure acts as follows. First a converged steady solution is obtained for a given refinement level. A global refinement indicator η_{glob} is then computed in order to estimate the accuracy of the obtained solution (e.g. total variation of entropy in a subsonic inviscid flow). This quantity is then compared to a user-defined threshold ω that specifies the desired level of

accuracy. Refinement is therefore deemed necessary if $\eta_{\text{glob}} > \omega$. In this case, element-wise refinement indicators η_K are computed and used to identify elements where the spatial resolution must be increased.

In this work, we use the maximum marking criterion. Namely, an element K is marked for refinement if :

$$\eta_K > \theta \max_{L \in \mathcal{T}_K} \eta_L \quad (10)$$

where $\theta \in [0, 1]$ is a user-defined marking parameter. Moreover, we have decided to limit to one the maximum change in polynomial degree between two neighbouring elements. For this reason additional elements may be marked for refinement.

Once the marking is completed, a new set of p values is computed by increasing by one the polynomial degree in marked elements. A maximum local polynomial degree is also specified by the user to avoid instability issues and/or the need for excessive memory storage. The simulation is then restarted from the previous solution based on this new set of p values.

The same procedure can be applied for static p -adaptation of unsteady periodic flows. In this case, the p -adaptive algorithm is applied once the periodic state of the flow is reached. A time-independent field must be defined in order to identify regions where increased spatial resolution is required in order to improve the accuracy of the simulation. In this work, the local refinement indicator is computed as the maximum of the instantaneous values of the error over a number of periods corresponding to the time interval T :

$$\eta'_K = \max_{t \in T} \eta_K(t) \quad (11)$$

where η_K is any error estimator computed from the instantaneous solution. Once these values have been computed, Eq. (10) can be applied by substituting η'_K in place of η_K to mark elements for refinement. Note that the instantaneous values $\eta_K(t)$ do not need to be computed at every discrete time step.

Other possible approaches could be defined in place of Eq. (11), e.g. by averaging in time the instantaneous refinement indicators or by applying error estimation techniques to the mean flow solution. Employing Eq. (11) has the advantage of removing the need for long integration times to obtain converged time-averaged values.

3.1. Review of refinement Indicators

In this section, the refinement indicators considered in this research are presented. First, three refinement indicators that can be classified as DE- or feature-based indicators are presented: the *VMS indicator*, the *spectral decay indicator* and the *non-conformity error indicator*. Second, two additional indicators will be introduced: the *residual-based* and *residuum-ncf based* indicator. These can be described as RE-based indicators.

3.1.1. The VMS indicator

The first refinement indicator that we consider in this work has been developed by Kuru et al. [1] in the context of the variational multiscale simulation (VMS) approach [32] and is defined as:

$$\eta_K := \left(\int_K \|(\rho \mathbf{v})_{h,p} - (\rho \mathbf{v})_{h,p-1}\|^2 dV \right)^{\frac{1}{2}} = \|(\rho \mathbf{v})_{h,p} - (\rho \mathbf{v})_{h,p-1}\|_{L^2(K)} \quad (12)$$

where $(\rho\mathbf{v})_{h,p-1}$ is the projection of the discrete momentum density on the reduced-order space S_h^{p-1} .

This refinement indicator acts as a DE estimate for $\mathbf{u}_{h,p}$ based on a lower-order solution. It can also be interpreted as a feature-based refinement indicator, measuring the ‘kinetic energy’ associated with the highest-order modes.

This estimator bears strong similarities with the error indicator developed by Mavriplis [16, 33] for which an additional term that depends on the decay rate of the modal coefficients is also included. The corresponding DE estimate developed, however, has been shown to produce relatively poor estimates of the exact DE for two- and three-dimensional problems [34]. For this reason, this indicator is not considered here.

As regards the original version of the VMS indicator, we have observed that poor results can be obtained from the use of this indicator when a mesh with large variation in element size in the domain is employed. In this work a normalized version of the VMS indicator is therefore considered, namely,

$$\eta_K^{VMS} := \left(\frac{\|(\rho\mathbf{v})_{h,p} - (\rho\mathbf{v})_{h,p-1}\|_{L^2(K)}^2}{|K|} \right)^{\frac{1}{2}} \quad (13)$$

where $|K|$ is the size of the element.

3.1.2. The spectral decay indicator

The so-called spectral decay indicator has been first introduced as a discontinuity sensor by Persson and Peraire [35] for shock capturing to stabilize numerical simulations in the presence of discontinuities. The spectral decay indicator, also known as smoothness indicator, is defined as:

$$S_e := \frac{\|f(\mathbf{u}_{h,p}) - f(\mathbf{u}_{h,p-1})\|_{L^2(K)}}{\|f(\mathbf{u}_{h,p})\|_{L^2(K)}} \quad (14)$$

where $\mathbf{u}_{h,p-1}$ represents the projection of the numerical solution on S_h^{p-1} and f is a function that depends on the solution. In [35], the authors have employed this smoothness indicator as a shock capturing parameter based on either the entropy or the enthalpy for $f(\mathbf{u})$. In successive works, Gassner et al. [36] have considered Eq. (14) based on the momentum density in one direction as a refinement indicator. Finally, Tumolo et al. [2, 37, 25, 27] have used this refinement indicator for the adaptive simulation of various CFD configurations. Following their approach, we define the spectral decay indicator as:

$$\eta_K^{SD} := \frac{\|(\rho\mathbf{v})_{h,p} - (\rho\mathbf{v})_{h,p-1}\|_{L^2(K)}}{\|(\rho\mathbf{v})_{h,p}\|_{L^2(K)}} \quad (15)$$

Note that Eq. (15) corresponds to the VMS indicator in Eq. (12) normalized by the total ‘energy’ in the cell defined by $\|(\rho\mathbf{v})_{h,p}\|_{L^2(K)}$.

3.1.3. The non-conformity error indicator

The third refinement indicator considered in this work is the so-called non-conformity (NCF) error. This indicator is based on the assumption that, unless a physical discontinuity is present, the exact solution is continuous across element faces. This implies that a jump in the numerical

solution can be considered as a measure of the error. For this reason, Krivodonova et al. [38, 39] have introduced the following discontinuity sensor:

$$\eta_K := \max_{\mathcal{E} \in \partial K} \max_j \left| \frac{\llbracket u_h(x_j) \rrbracket}{2\{\{u_h(x_j)\}\}} \right| \quad (16)$$

where u_h is a variable, such as the density or the pressure, and x_j are the positions of the quadrature points on the element faces. This error estimator can also be considered as a local DE estimator thanks to the superconvergent phenomena at outflow boundaries exhibited by some particular formulations of the DG method [38, 39]. Gassner and Altmann [36] have employed this quantity as a refinement indicator. Following their approach, we indicate as non-conformity error indicator:

$$\eta_K^{NCF} := \max_{\mathcal{E} \in \partial K} \max_j \frac{\|(\rho \mathbf{v}_h)^+(x_j) - (\rho \mathbf{v}_h)^-(x_j)\|}{2\|\{\{(\rho \mathbf{v}_h)(x_j)\}\}\|} \quad (17)$$

3.1.4. The residual-based indicator

The residual-based refinement indicator described here follows from the classical derivation of residual-based error estimators for FE methods [40] and that by Hartmann and Houston [41]. Let us write the semidiscrete form of Eq. (6) as:

$$\mathcal{N}_h(\mathbf{u}_h, \phi) = 0 \quad \forall \phi \in S_h^p \quad (18)$$

and let $J(\mathbf{u})$ be a nonlinear target functional. Provided that the target functional satisfies a compatibility condition and the discretized operator is adjoint consistent [21], it is possible to show that:

$$J(\mathbf{u}) - J(\mathbf{u}_h) = -\mathcal{N}_h(\mathbf{u}_h, z) \quad (19)$$

where z is the solution of an adjoint problem derived from the target functional $J(\mathbf{u})$. The derivation of this result corresponds to the general derivation of duality-based *a posteriori* error estimators. Manipulating the semidiscrete operator Eq. (18), it is possible to obtain:

$$\mathcal{N}_h(\mathbf{u}_h, \phi) = \sum_{K \in \mathcal{T}_K} \left[\int_K \mathbf{R}(\mathbf{u}_h) \phi dV + \int_{\partial K \cap \mathcal{E}_i} \mathbf{r}(\mathbf{u}_h) \phi^+ dS + \int_{\partial K \cap \mathcal{E}_b} \mathbf{r}_b(\mathbf{u}_h) \phi^+ dS \right] \quad (20)$$

in which the terms on the right-hand side are defined as:

$$\mathbf{R}(\mathbf{u}_h) = \frac{\partial \mathbf{u}_h}{\partial t} + \nabla \cdot \mathcal{F}_c(\mathbf{u}_h) - \nabla \cdot \mathcal{F}_v(\mathbf{u}_h, \nabla_h \mathbf{u}_h + \mathbf{L}_h) \quad (21)$$

$$\mathbf{r}(\mathbf{u}_h) = \left[H_c(\mathbf{u}_h^+, \mathbf{u}_h^-, \mathbf{n}) - \mathcal{F}_c(\mathbf{u}_h^+) \cdot \mathbf{n} \right] - \left[\{\{\mathcal{F}_v(\mathbf{u}_h, \nabla_h \mathbf{u}_h + \eta_e r_h^e)\}\} - \mathcal{F}_v(\mathbf{u}_h^+, \nabla_h \mathbf{u}_h^+ + \mathbf{L}_h) \right] \cdot \mathbf{n} \quad (22)$$

$$\mathbf{r}_b(\mathbf{u}_h) = \left[\mathcal{F}_c(\mathbf{u}_b) - \mathcal{F}_c(\mathbf{u}_h^+) \right] \cdot \mathbf{n} - \left[\mathcal{F}_v(\mathbf{u}_b, \nabla_h \mathbf{u}_b + \eta_e r_h^e) - \mathcal{F}_v(\mathbf{u}_h^+, \nabla_h \mathbf{u}_h^+ + \mathbf{L}_h) \right] \cdot \mathbf{n} \quad (23)$$

In Eq. (21) to (23), $\mathbf{R}(\mathbf{u}_h)$ measures how accurately the numerical solution within an element satisfies the (continuous) mathematical model, the inter-element residual $\mathbf{r}(\mathbf{u}_h)$ measures the jump in the convective and viscous fluxes at the internal faces, and the boundary residual $\mathbf{r}_b(\mathbf{u}_h)$ measures the error in the imposition of the boundary conditions.

Provided that the adjoint solution is $z|_K \in H^s(K)$ with $2 \leq s \leq p + 1, \forall K \in \mathcal{T}_K$, it can be shown [21] that the error in the target functional is bounded by

$$|J(\mathbf{u}) - J(\mathbf{u}_h)| \leq C_{\text{int}} \left(\sum_{K \in \mathcal{T}_K} \eta_K^2 \right)^{\frac{1}{2}} \quad (24)$$

with C_{int} a positive constant which depends on the regularity of the mesh, the polynomial degree p and the regularity of the dual solution, and

$$\eta_K := h_K^s \|\mathbf{R}(\mathbf{u}_h)\|_{L^2(K)} + h_K^{s-\frac{1}{2}} \|\mathbf{r}(\mathbf{u}_h)\|_{L^2(\partial K \cap \mathcal{E}_i)} + h_K^{s-\frac{1}{2}} \|\mathbf{r}_b(\mathbf{u}_h)\|_{L^2(\partial K \cap \mathcal{E}_b)} \quad (25)$$

On the basis of numerical experiments, Hartmann and Houston have actually employed the following residual-based indicator:

$$\eta_K^{RB} := h_K \|\mathbf{R}(\mathbf{u}_h)\|_{L^2(K)} + h_K^{\frac{1}{2}} \|\mathbf{r}(\mathbf{u}_h)\|_{L^2(\partial K \cap \mathcal{E}_i)} + h_K^{\frac{1}{2}} \|\mathbf{r}_b(\mathbf{u}_h)\|_{L^2(\partial K \cap \mathcal{E}_b)} ; \quad \eta_{\text{glob}} := \left(\sum_{K \in \mathcal{T}_K} \eta_K^2 \right)^{\frac{1}{2}} \quad (26)$$

In the work presented in this paper, a normalized variant of this indicator is also considered:

$$\eta_K^{RBN} := \|\mathbf{R}(\mathbf{u}_h)\|_{L^2(K)} + h_K^{-\frac{1}{2}} \|\mathbf{r}(\mathbf{u}_h)\|_{L^2(\partial K \cap \mathcal{E}_i)} + h_K^{-\frac{1}{2}} \|\mathbf{r}_b(\mathbf{u}_h)\|_{L^2(\partial K \cap \mathcal{E}_b)} \quad (27)$$

3.1.5. The residuum-NCF based indicator

In [42] Dolejší has proposed a refinement indicator based on the following global error definition:

$$E := \left(R(\mathbf{u}_h)^2 + \text{NCF}(\mathbf{u}_h)^2 \right)^{\frac{1}{2}} \quad (28)$$

where $R(\mathbf{u}_h)$ is called residuum error and $\text{NCF}(\mathbf{u}_h)$ is a measure of the non-conformity error.

Denoting by $X := H^2(\Omega, \mathcal{T}_K) = \{ \phi : \phi \in H^2(K), \forall K \in \mathcal{T}_K \}$ the broken Sobolev space, these quantities are defined as:

$$R(\mathbf{u}_h) := \|\mathcal{N}_h(\mathbf{u}_h, \cdot)\|_X = \sup_{\phi \in X \setminus \{0\}} \frac{\|\mathcal{N}_h(\mathbf{u}_h, \phi)\|}{\|\phi\|_X} \quad (29)$$

$$\text{NCF}_K(\mathbf{u}_h) := \int_{\partial K \in \mathcal{E}_i} h_{\partial K}^{-1} \|\llbracket \mathbf{u}_h \rrbracket\|^2 dS + \int_{\partial K \in \mathcal{E}_b} h_{\partial K}^{-1} (\mathbf{u}_h - \mathbf{u}_b)^2 dS ; \quad \text{NCF}(\mathbf{u}_h) := \left(\sum_{K \in \mathcal{T}_K} \text{NCF}_K^2(\mathbf{u}_h) \right)^{\frac{1}{2}} \quad (30)$$

For the analytical solution we have that $\mathcal{N}_h(\mathbf{u}, \phi) = 0, \forall \phi \in X$, while for the numerical solution this is true only for $\phi \in S_h^p$, thus the residuum error is a measure of the residual in the weak form of Eq. (1).

Using Eq. (19) and Eq. (29), it can be readily shown that

$$|J(\mathbf{u}) - J(\mathbf{u}_h)| = |\mathcal{N}_h(\mathbf{u}_h, z)| \leq R(\mathbf{u}_h) \|z\|_X \quad (31)$$

Therefore, limiting the residuum error has a similar effect to limiting the residual-based indicator defined in Eq. (25) in the evaluation of the error in a target functional. The residuum error

cannot be exactly computed, as it is defined on an infinite-dimensional space. Thus, the residuum error estimator and the local or element-wise residuum error estimator are used in practice and are defined as:

$$\rho_h(\mathbf{u}_h) := \sup_{\phi \in S_h^{p+1} \setminus \{0\}} \frac{\|\mathcal{N}_h(\mathbf{u}_h, \phi)\|}{\|\phi\|_X} \quad (32)$$

$$\rho_{h,K}(\mathbf{u}_h) := \sup_{\phi \in S_K^{p+1} \setminus \{0\}} \frac{\|\mathcal{N}_h(\mathbf{u}_h, \phi)\|}{\|\phi\|_X} \quad (33)$$

The spaces S_h^{p+1} and S_K^{p+1} correspond, respectively, to the space of piecewise polynomials of maximum degree $p + 1$ and its restriction to the considered element K for the evaluation of the local residuum error estimator, defined by:

$$S_K^{p+1} := \left\{ \phi \in L^2(K) : \phi|_K \in \mathcal{P}^{p+1}(K), \phi|_{K'} = 0, \forall K, K' \in \mathcal{T}_k, K \neq K' \right\} \quad (34)$$

As regards the norm $\|\cdot\|_X$ employed in this work, following Dolejší [42], we use the following definition

$$\|\cdot\|_X := \left(\|\cdot\|_{L^2(\Omega)}^2 + \frac{1}{\text{Re}} |\cdot|_{H^1(\Omega, \mathcal{T}_K)}^2 \right)^{\frac{1}{2}} \quad (35)$$

where Re is the Reynolds number and $|\cdot|_{H^1}$ is the broken Sobolev seminorm. Other norms have also been employed in the literature [43, 44]. It can be shown (see [43]) that, based on this choice, the residuum error estimator can be directly computed from the element-wise values, namely,

$$\rho_h(\mathbf{u}_h)^2 = \sum_{K \in \mathcal{T}_K} \rho_{h,K}(\mathbf{u}_h)^2 \quad (36)$$

The residuum-NCF refinement indicator therefore takes the final form:

$$\eta_K^{\text{NCF}} := \left(\rho_{h,K}(\mathbf{u}_h)^2 + \text{NCF}_K(\mathbf{u}_h)^2 \right)^{\frac{1}{2}} ; \quad \eta_{\text{glob}} := \left(\sum_{K \in \mathcal{T}_K} \eta_K^2 \right)^{\frac{1}{2}} = \left(\rho_h(\mathbf{u}_h)^2 + \text{NCF}(\mathbf{u}_h)^2 \right)^{\frac{1}{2}} \quad (37)$$

In order to evaluate this indicator, the local residuum estimator $\rho_{h,K}(\mathbf{u}_h)$ is computed by seeking a solution of the form $\psi = \sum_{i=1}^{N_{p+1}} \xi_i \phi_i$, where $\{\phi_i\}_{1 \leq i \leq N_{p+1}}$ is a basis for S_K^{p+1} and ξ_i are the unknown coefficients, such that $|\mathcal{N}_h(\mathbf{u}_h, \psi)|$ is maximum and $\|\psi\|_X = 1$. This leads to a constrained optimisation problem which can be solved via the Lagrange multipliers technique, which requires the computation of the residuals $\mathcal{N}_h(\mathbf{u}_h, \phi_i)$.

It should be noted that $\mathcal{N}_h(\mathbf{u}_h, \psi)$, $\forall \psi \in S_K^p$ should be identically null by virtue of the Galerkin orthogonality property. In practice this is not the case due to the presence of an algebraic error which is the combination of the aliasing and, for steady problems, iterative errors. Thus, in order to evaluate this contribution, we compute the quantity $\mathcal{N}_h(\mathbf{u}_h, \psi)$ by using an increased number of quadrature points compared to the ones used to compute \mathbf{u}_h .

4. Evaluation of the performance of refinement indicators

In this section we present the results from the application of adaptive p -refinement based on the indicators described above. Firstly, we consider the inviscid flow over a Gaussian bump at Mach number $M = 0.5$. Secondly, we analyse two laminar steady configurations: the laminar flow past a Joukowski airfoil at Reynolds number $Re = 1000$ and $M = 0.5$, and the laminar flow past a cylinder at $Re = 40$ and $M = 0.1$. Finally, the p -adaptation methodology developed in this research is applied to the unsteady periodic laminar flow past a cylinder at $Re = 100$ and $M = 0.1$.

In order to compare the different refinement indicators considered, we proceed in the following way. The p -adaptive algorithm is applied starting from the solution corresponding to a uniform polynomial degree $p = p_{\min}$ and limiting the maximum polynomial degree to a user-defined value p_{\max} . At each iteration of the algorithm, a new distribution of polynomial degrees is defined based on local error estimates (as explained in Sec. 3) and a new numerical solution is computed.

In order to determine whether the p -adaptive algorithm is converged different approaches can be considered. One approach consists in the definition of a global error indicator, η_{glob} , which can be derived from the element-wise error estimates η_K as seen in Sec. 3. However this choice would lead to different measures of accuracy and convergence criteria for the refinement indicators analysed. In order to simplify the comparison, the accuracy of the adaptive solution and the convergence of the adaptive algorithm are measured by evaluating the error in the computation of prescribed target quantities. As the maximum polynomial degree is limited, the maximum local spatial resolution is also bounded and the highest possible accuracy produced by the adaptive algorithm is the same as that corresponding to uniform polynomial degree $p = p_{\max}$, albeit with a reduced number of DOFs. The p -adaptive algorithm is therefore considered converged when, for all quantities of interest, the same accuracy as that of the simulation with uniform polynomial degree $p = p_{\max}$ is achieved. The reduction in computational cost provided by adaptive refinement are then measured by comparing the results from the p -adaptive simulations with those obtained from uniform p -refinement.

In order to identify possible advantages or drawbacks of different refinement indicators, we also analyse the maps of polynomial degrees obtained at a similar number of DOFs. This allows us to identify the different regions selected by the adaptive algorithm and provides useful information on the sensitivity of some indicators to mesh quality, the marking algorithm or specific features of the flow. Repeating this analysis for different test cases allows us to corroborate our observations and therefore to draw general conclusions from our study.

Table 1 compiles the main parameters that have been employed in the adaptive algorithm for the considered test cases. We further note that all simulations have been performed by employing $q = p + 5$ quadrature points in each spatial direction. This is necessary to avoid aliasing errors arising from the quadrature due to the non-linear convective terms and the use of high-order curved meshes. For each simulation we have verified that further increasing this value has a negligible effect on the results.

4.1. Steady Euler flow over a Gaussian Bump

The first test case considered is the inviscid flow over a Gaussian bump at $M = 0.5$, widely studied at the series of *International Workshops of High-Order CFD Methods* (HiOCFD) [45]. The configuration is 2D and consists of a subsonic inlet and an outlet with a prescribed static

	Physical model	p_{\min}	p_{\max}	θ	Target quantity
Case 1	Euler steady	2	4	0.5	entropy error
Case 2	N-S steady	2	5	0.1	$C_D, \ (\rho\mathbf{v}) - (\rho\mathbf{v})_{\text{ref}}\ _{L^2(\Omega)}$
Case 3	N-S steady	2	6	0.5	$C_D, \ (\rho\mathbf{v}) - (\rho\mathbf{v})_{\text{ref}}\ _{L^2(\Omega)}$
Case 4	N-S unsteady	2	6	0.1	$\overline{C_D}, C'_L, St$

Table 1: Numerical parameters for the p -adaptive algorithm.

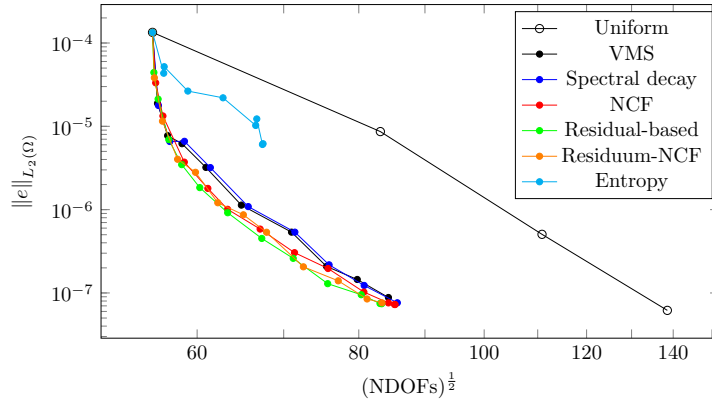


Figure 1: Euler flow over a Gaussian bump at $M = 0.5$: evolution of global entropy error Eq. (38) under uniform and adaptive refinement.

pressure. Slip boundary conditions are imposed at the upper and bottom walls. The mesh employed in the simulations presented here is a 4th-order mesh which is generated based on the analytical expression of the bump corresponding to a Gaussian profile.

The accuracy of the performed simulations is measured by the entropy error on the full domain, namely:

$$\|e\|_{L^2(\Omega)}^2 = \int_{\Omega} \left(\frac{p}{p_{\infty}} \left(\frac{\rho_{\infty}}{\rho} \right)^{\gamma} - 1 \right)^2 d\Omega \quad (38)$$

where p_{∞} and ρ_{∞} are the static pressure and density corresponding to the prescribed inlet conditions. For inviscid subsonic flows with uniform inlet conditions no entropy variations are expected in the domain. This quantity $\|e\|_{L^2}$ therefore represents an exact measure of the discretization error.

Figure 1 shows the variation of this error measure versus the number of DOFs when uniform p -refinement is performed (solid black line with circles) as well as for the locally p -adapted simulations (coloured curves with dots). For the latter, we report the results based on the refinement indicators introduced in the previous section with the exception of the normalized variant of the residual-based indicator Eq. (27). Indeed, in this case the residual-based indicator and its normalized variant provide identical results due to the very limited variation of the characteristic element size of the mesh employed. As reference, we also report the results obtained by using the local entropy error as refinement indicator (light blue dots in Fig. 1). Figure 2 shows the maps of local polynomial degree at the last iteration of the refinement procedure for the six indicators considered.

As seen from Fig. 1 and 2a, the results obtained for the local entropy error indicator illustrate

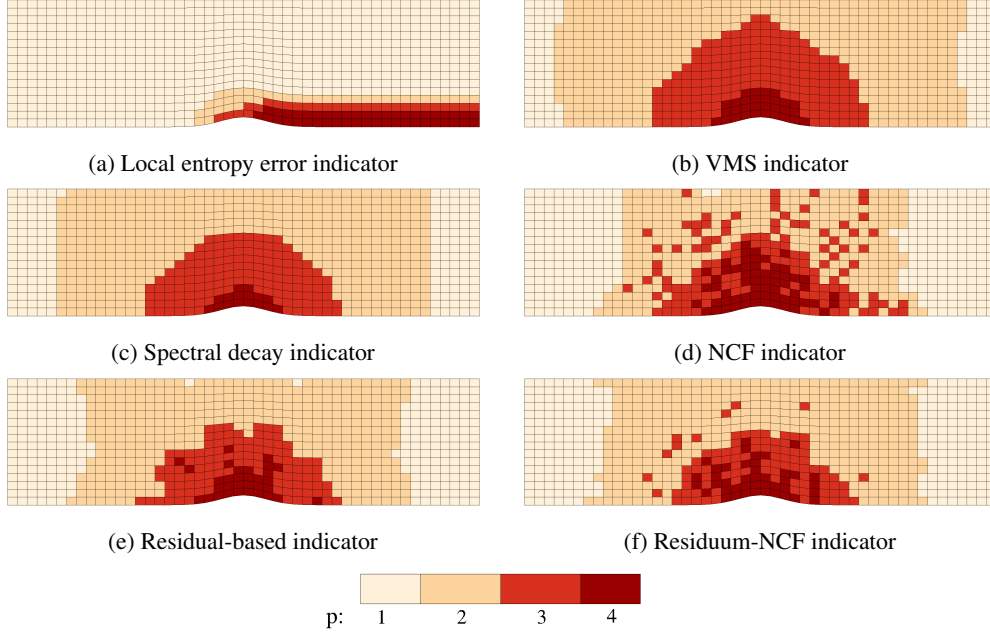


Figure 2: Euler flow over a Gaussian bump at $M = 0.5$: map of local polynomial degrees obtained based on different refinement indicators.

one of the possible drawbacks of DE-based refinement indicators as mentioned in Sec. 1. In fact, for this configuration it is expected that a higher spatial resolution is required in the proximity of the bump. In underresolved simulations an error in the entropy is produced in this region and is convected downstream. For this reason, as can be seen in Fig. 2a, this refinement indicator effectively selects for further refinement the region behind the bump. This is the cause of the suboptimal performance exhibited by this estimator, as seen in Fig. 1.

In spite of their very different formulation, implementation and computational cost, the other refinement indicators show very similar behaviour. The residual-based, residuum-NCF and NCF refinement indicators show slightly better performance after the initial refinement step. The residual-based indicator leads to a reduction in the number of DOFs necessary to achieve the same convergence level as the uniform $p = 4$ simulation of approximately 63%. In the case of the VMS and spectral decay indicators the savings in terms of DOFs are of about 58%. It is also interesting to note that, despite being DE estimators, the VMS, spectral decay and NCF indicators do not share the deficiencies exhibited by the local entropy error indicator. A possible explanation for this is that the production of errors is concentrated in the high-frequency content of the solution. By definition, the above mentioned indicators identify regions where the largest amount of energy is contained in the high-frequency content of the solution thus selecting for refinement regions where errors are being generated rather than those where they have been convected.

Coming back to Fig. 2, we observe that the VMS and spectral decay indicators produce almost identical maps of local polynomial degree. The residual-based, residuum-NCF and NCF indicators also provide refinement patterns which are very similar to each other. By comparing

these to the pattern shown by the VMS indicator, we can observe that they present a smaller refinement region while the number of elements with higher polynomial degree is increased. As expected, the residuum-NCF indicator generates a polynomial degree map which is in between the ones produced by the residual-based and the NCF-based estimators. Finally, it is worth noting the checkerboard-like pattern generated by the NCF indicator and to some extent the residuum-NCF indicator. This is despite the initial smooth distribution of the refinement indicator at the beginning of the adaptive procedure. Through numerical experiments, we have observed that this pattern appears to be strongly influenced by the refinement history. Indeed modifying the marking algorithm or its parameters actually leads to the generation of a different checkerboard-like pattern. A much weaker influence has been observed for the refinement levels generated by the other refinement indicators.

4.2. Steady laminar flow past a Joukowski airfoil

The first laminar test case considered is the flow past a symmetric Joukowski airfoil at zero incidence ($\alpha = 0^\circ$), $M = 0.5$ and $\text{Re} = 1000$ based on the chord length. This configuration has been proposed as a test case of the 4th and 5th HiOCFD [46, 47]. The flow field is two-dimensional laminar and symmetric. The solution is free of shocks or recirculation bubbles but the cusped trailing edge introduces a geometric singularity which could negatively impact the convergence rate of the p -refinement algorithm. It is therefore interesting to investigate how the different refinement indicators deal with this singularity.

4.2.1. Computational details

The simulations presented here are performed by considering a computational domain defined by a semicircular region of radius $R = 100$ chords centered at the leading edge, followed by a rectangular region extending up to 100 chords from the trailing edge. The dynamic viscosity coefficient is taken constant, adiabatic wall boundary conditions are imposed on the airfoil and non-reflecting conditions are imposed at the external boundaries. From numerical experiments, we know that this extent of the computational domain is not sufficient to obtain a solution completely independent of the imposed far-field boundary conditions. However, in our numerical tests the artificial boundary does not appear to have a negative effect on the numerical solution.

All computations are performed using one of the meshes provided by the 4th HiOCFD [46].¹ We note that this mesh is characterized by a strong refinement localized in proximity of the trailing edge. This limits the harmful effect of the geometrical singularity on the convergence rate of the simulation.

In order to compare the accuracy of the adapted solutions obtained based on the different indicators, we consider the convergence history of both the error in the drag coefficient and in the L^2 -norm of momentum density. These error quantities are computed by considering as reference the numerical solution obtained with uniform polynomial degree $p = 7$. It has been verified that the drag coefficient computed from this reference solution ($C_D = 0.1219$) is in agreement with the results reported in [46, 47].

The next section presents the main results obtained from the p -adaptive simulations.

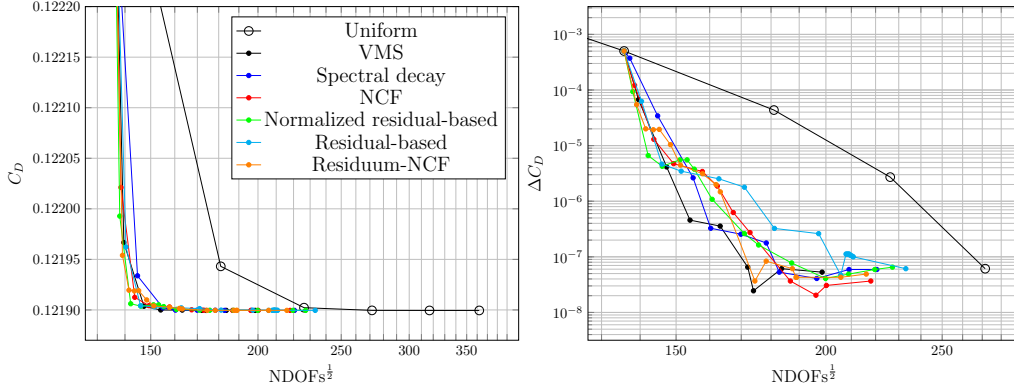


Figure 3: Laminar flow past a Joukowski airfoil, $Re = 1000$, $M = 0.5$, $\alpha = 0^\circ$: Convergence history of the drag coefficient under uniform and adaptive p -refinement.

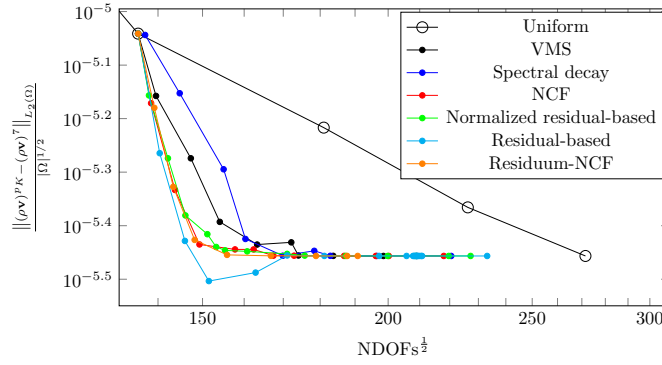


Figure 4: Laminar flow past a Joukowski airfoil, $Re = 1000$, $M = 0.5$, $\alpha = 0^\circ$: L^2 -norm of the error in momentum density under uniform and adaptive p -refinement.

4.2.2. Analysis of the p -adaptive results

Figures 3 and 4 show the convergence history of the drag coefficient (Fig. 3a) and its corresponding error (Fig. 3b) as well as the L^2 -norm of the error in momentum density (Fig. 4) under uniform and adaptive p -refinement. From these figures, we can observe that for a target value of the error in the drag coefficient, $\Delta C_D = 10^{-7}$, most refinement indicators achieve a reduction in the number of DOFs with respect to the uniform refinement of approximately 53%. Only the residual-based indicator leads to a smaller reduction of about 30%.

These results show that, among the considered error estimators, the VMS indicator produces the fastest reduction of the error in the drag coefficient, followed by the spectral decay, NCF, residuum-NCF and normalized residual-based indicator. By analysing the L^2 -norm of the error in the momentum density we can observe however that the standard residual-based indicator exhibits the best performance, with the VMS and spectral decay indicators providing the slowest

¹The mesh employed corresponds to the first refinement level of the mesh composed of 4th-order quads that can be found on [46].

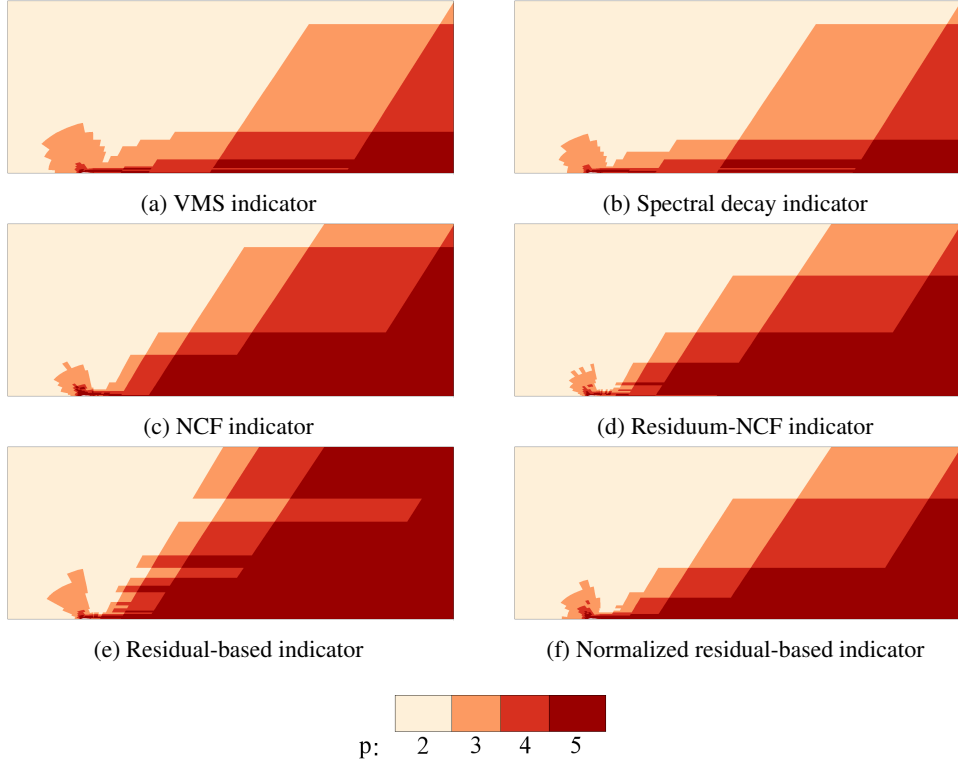


Figure 5: Laminar flow past a Joukowski airfoil, $Re = 1000$, $M = 0.5$, $\alpha = 0^\circ$: Local polynomial degree distribution obtained for different refinement indicators.

convergence. Nonetheless, in terms of number of DOFs required to achieve the target error level, very small differences are found between the different error indicators.

These results clearly illustrate that in order to draw meaningful conclusions from the comparison of different refinement techniques it is necessary to consider more than one error measure. Moreover, it is essential to look at the full convergence history, as considering only isolated values of the error measure can lead to misleading results.

The different performance observed between the different indicators can be better analysed by studying the maps of polynomial degrees (Fig. 5 and a close up in the region around the airfoil in Fig. 6) obtained at a similar number of DOFs (for this particular example $NDOFs^{\frac{1}{2}} \approx 180$). As seen from Fig. 3, at this refinement level the p -adaptive algorithm has achieved the target level of accuracy for all refinement indicators, with the exception of the standard residual-based indicator. In Fig. 5 and 6 we observe that the maps of the distribution of polynomial degrees corresponding to the VMS and spectral decay indicators are almost identical. This was also the case for the Euler configuration considered in section 4.1. For the present configuration however, the spectral decay indicator presents higher refinement levels, compared to the VMS indicator, in the proximity of the trailing edge. This behaviour suggests a strong sensitivity of this indicator to the presence of singularities in the solution. The normalized residual-based indicator also appears to be sensitive to the presence of the singularity, while all other refinement indicators

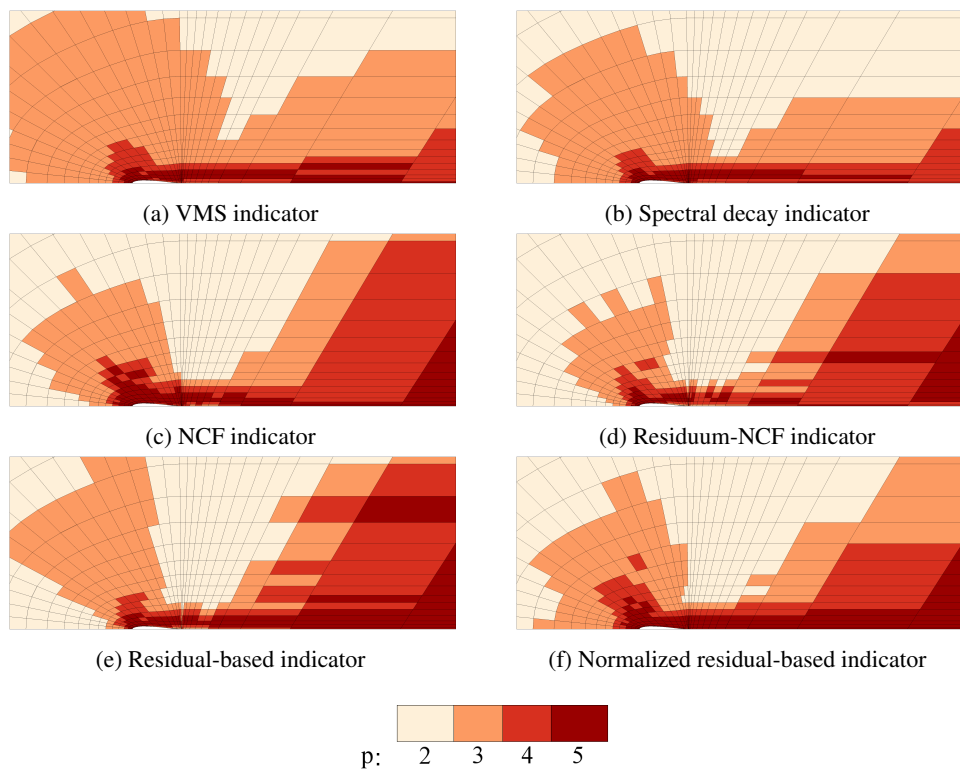


Figure 6: Laminar flow past a Joukowski airfoil, $Re = 1000$, $M = 0.5$, $\alpha = 0^\circ$: Close up view of local polynomial degree distribution obtained for different refinement indicators.

select for refinement this region only after several refinement steps. Further testing would be required in order to assess the generality of these results.

Moreover, we can observe from Fig. 5 that, compared to other indicators, the VMS and spectral decay indicators generate a larger refinement region upstream of the airfoil and lower refinement levels in the far-wake region. This behaviour can explain the results shown in Fig. 3 and 4. As seen in these figures, the VMS and spectral decay indicators produce a faster reduction of the error in the drag coefficient by increasing, in the initial refinement steps, the spatial resolution in the upstream region and in the proximity of the airfoil (see Fig. 5a and 5b). In contrast, all the other considered indicators introduce stronger refinement in the far-wake region (Fig. 5c-f) which is characterized by large and rapid variation of element size and high aspect ratio. This poor mesh quality is possibly the source of high values of the error in the momentum density in the far-wake region. Thus increasing the spatial resolution in this region can improve this error measure even if it has a minor effect on the error in the drag coefficient. In particular, among all considered indicators, the residual-based indicator shows the strongest sensitivity to mesh quality and mesh size.

Similar conclusions can be drawn by analysing the maps of error distribution. As an example we report in Fig. 7 the distribution of the considered refinement indicators evaluated for the solution obtained with a uniform polynomial degree $p = 2$. For completeness the element-wise L^2 -norm of the error in momentum density is also presented (Fig. 7g).

Finally, we note that the checkerboard-like pattern displayed by the NCF and residuum-NCF indicators in the Euler test case can also be observed in Fig. 5 and 6 as well as at intermediate steps of the p -adaptive algorithm (not shown here).

4.3. Steady laminar flow past a cylinder at $Re = 40$

The second viscous flow configuration considered is the laminar flow past a circular cylinder at $Re = 40$ and $M = 0.1$. For the considered Reynolds number the flow field is two-dimensional, symmetric and steady. The flow separates leading to the formation of two recirculation bubbles in the near wake that need to be correctly resolved in order to compute the drag coefficient accurately. This configuration therefore constitutes an interesting test case for the validation of CFD codes.

4.3.1. Numerical details

Two-dimensional simulations are thus performed by imposing no-slip boundary conditions at the wall and non-reflecting boundary conditions on the external boundary.

Extensive research has been dedicated in the literature to the analysis of the effect of the size of the computational domain on the solution of this unbounded flow. It has been shown that the presence of the artificial boundary is responsible for blockage effects and can distort phenomena generated in the internal domain and convected through the artificial boundary [48, 49]. In this research, a computational domain of radius $R = 2000D$ is therefore employed. For this extension of the computational domain, it has been verified that the effect of the external boundary on the drag coefficient is of the order of $\mathcal{O}(10^{-5})$.

The mesh employed for the following simulations is an O-type 4th-order mesh with 18 and 28 elements in the radial and azimuthal directions respectively. In the radial direction the element size changes following a geometric progression of ratio 1.25 up to $r = 6D$ and 1.65 up to the external boundary.

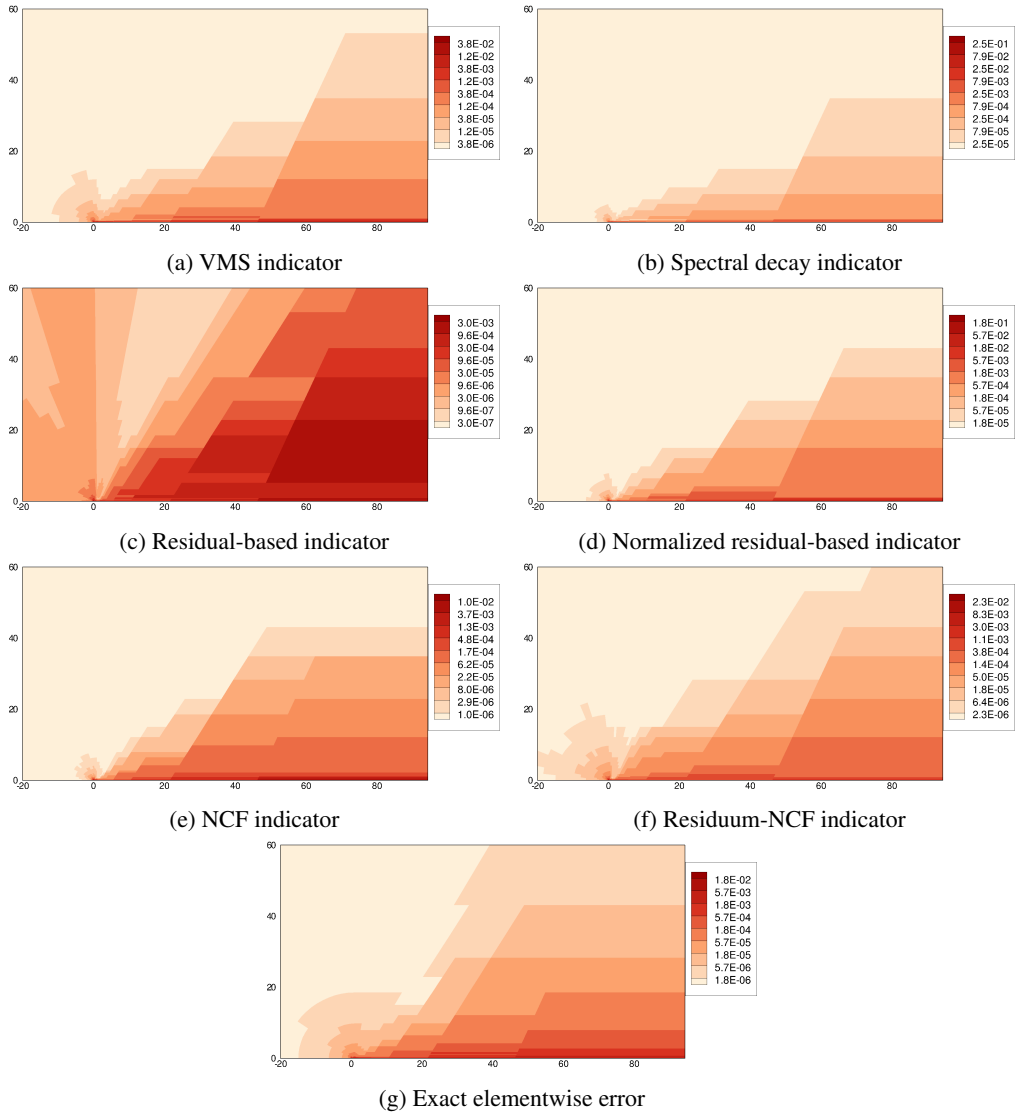


Figure 7: Laminar flow past a Joukowski airfoil, $Re = 1000$, $M = 0.5$, $\alpha = 0^\circ$: Error and refinement indicators for uniform polynomial degree $p = 2$.

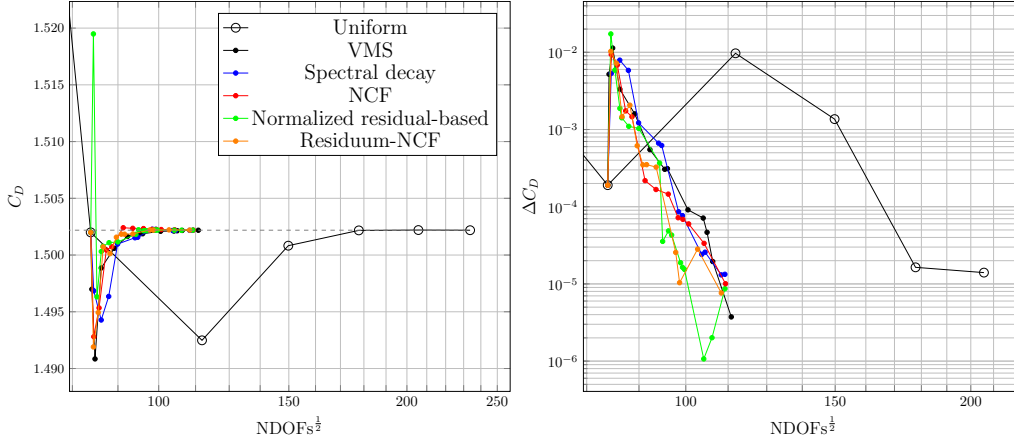


Figure 8: Laminar flow past a cylinder, $\text{Re} = 40$, $M = 0.1$: Evolution of the drag coefficient and corresponding error under uniform and adaptive p -refinement.

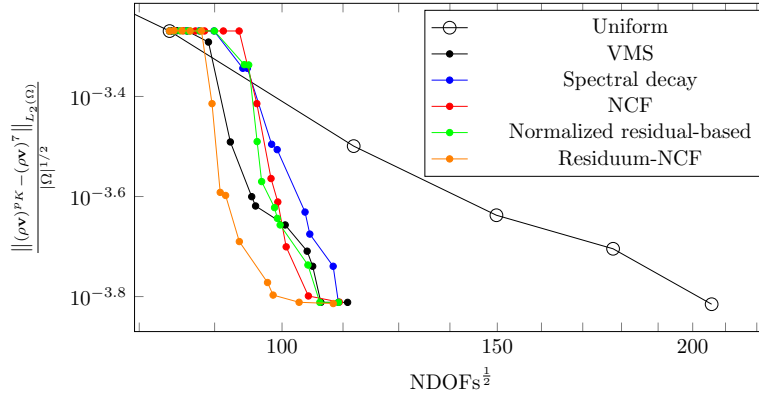


Figure 9: Laminar flow past a cylinder, $\text{Re} = 40$, $M = 0.1$: L^2 -norm of the error in the momentum density under uniform and adaptive p -refinement.

Given the slow convergence in the drag coefficient observed for the standard residual-based indicator in the previous configuration, only its normalized version is considered for this test case.

4.3.2. Analysis of the p -adaptive results

Figures 8 and 9 show the evolution of the error in the drag coefficient and in the L^2 -norm of the momentum density using uniform and adaptive p -refinement with respect to a reference solution obtained with uniform $p = 7$ for which $C_D = 1.5022$.

All refinement indicators are able to reduce by about 75% the number of DOFs necessary to achieve the same accuracy as that provided by a uniform polynomial degree $p = 6$. These results fall in line with those obtained in the previous test case, with all refinement indicators leading to a comparable computational gain in terms of numbers of DOFs. If we consider the error in the drag coefficient shown in Fig. 8b, we can observe that the normalized residual-based and the

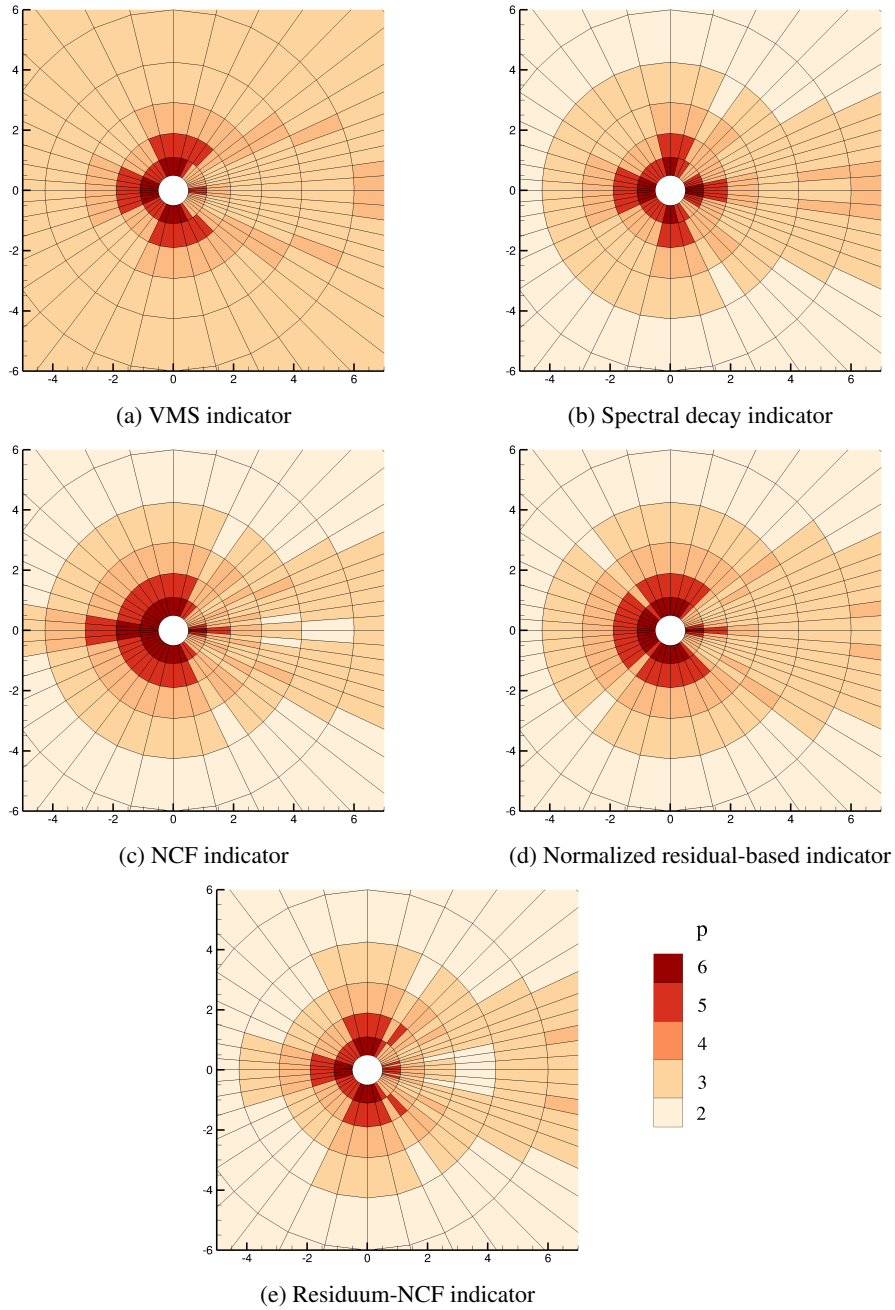


Figure 10: Laminar flow past a cylinder, $Re = 40$, $M = 0.1$: Local polynomial degree distribution obtained with different refinement indicators.

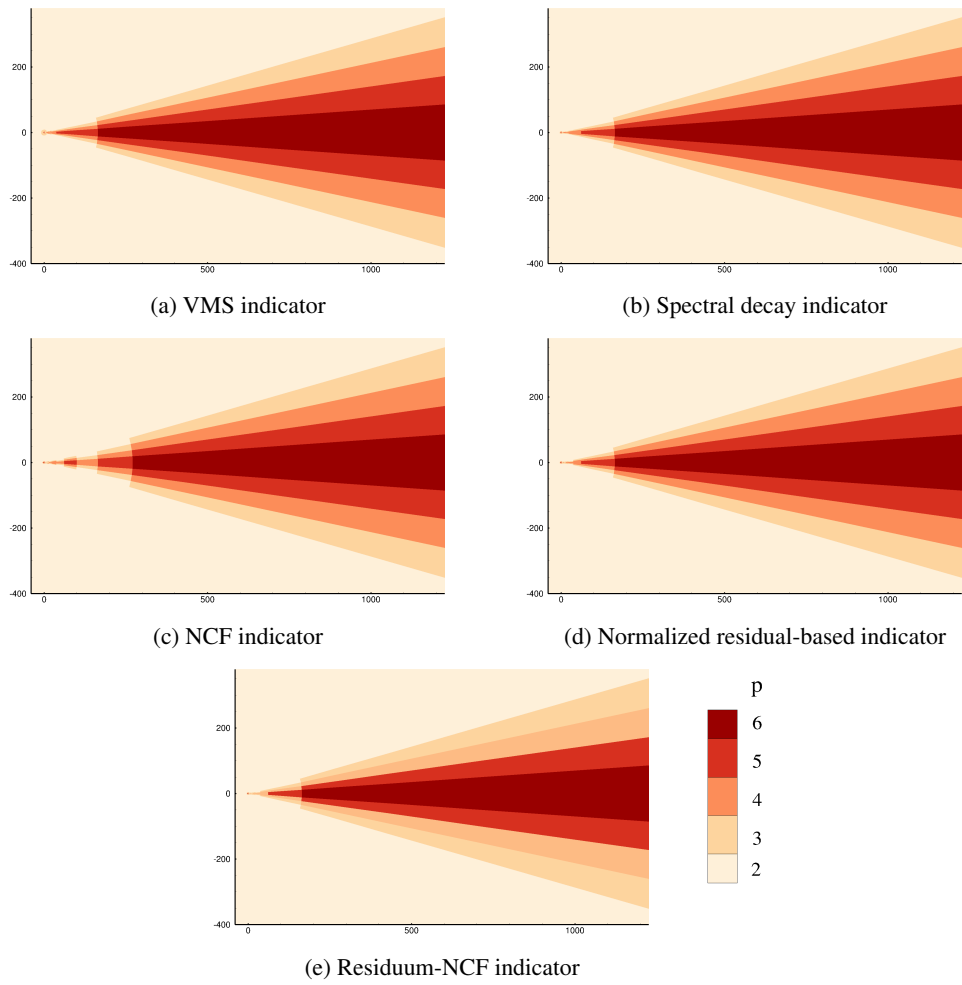


Figure 11: Laminar flow past a cylinder, $Re = 40$, $M = 0.1$: Local polynomial degree distribution obtained with different refinement indicators.

residuum-NCF refinement indicators show slightly better performance than the other indicators considered. On the other hand, for the previous configuration the fastest convergence of the drag coefficient has been obtained using the VMS and spectral decay indicator (Fig. 3). Nonetheless, for this test case only minor differences can be observed and do not indicate a clear advantage in the use of one of the refinement indicators. As regards the discretization error plotted in Fig. 9, the residuum-NCF refinement indicator and the VMS estimator appear to lead to the fastest convergence, with the residuum-NCF indicator performing best.

It is also interesting to inspect the maps of the distribution of local polynomial degrees corresponding to the last iteration of the adaptive refinement procedure for different estimators. For this last iteration, the number of degrees of freedom is approximately 12000 ($\text{NDOFs}^{\frac{1}{2}} \approx 110$). These are shown in Fig. 10 and 11. While some differences can be observed between the different maps, the distributions of local polynomial degree are overall fairly similar for all the considered refinement indicators. As an example, all the indicators appear to select for refinement an approximately circular region around the cylinder as well as the shear region extending up to the outer boundary. Moreover, they all select for further refinement the regions right upstream of the cylinder and those located at an angle of 90° , before the separation of the flow which is located at 125° [48].

One of the main differences that can be observed is the disparity in the refinement levels obtained in the recirculation region and in proximity of the cylinder base. Among all refinement indicators, the VMS and spectral decay indicators lead respectively to the lowest and highest refinement levels in this region. This different behaviour between the VMS and spectral decay indicators, already observed in the previous configuration, is somewhat expected. Indeed the spectral decay indicator is based on a normalized estimate of DE by using the total ‘energy’ of the flow and therefore tends to select for further refinement regions that are characterized simultaneously by lower values of the error and of the ‘energy’ (e. g. recirculation regions or stagnation points). This difference could be the cause of the slower convergence rate demonstrated by the spectral decay indicator in terms of the L_2 -norm of the error in the momentum density.

As already mentioned above, all refinement indicators select for refinement the far-wake region extending to the outer boundary. This is certainly due to the large size of the elements in this region requiring an increase in polynomial degree in order to correctly represent the flow. We can see from Fig. 9 that this increase in refinement level leads to a reduction of the L_2 -norm of the error in the momentum density even though the effect on the convergence of the drag coefficient is rather limited as can be seen in Fig. 8. This behaviour can be compared with the one observed in the previous test case in Fig. 7. Indeed for the adaptive simulation of the laminar flow past a Joukowski airfoil, different refinement levels have been obtained in the far-wake region depending on the refinement indicator employed, while the same refinement levels have been obtained for this configuration. This difference can be explained by a stronger sensitivity of the NCF, residuum-NCF and normalized residual-based indicators to rapid variations of the mesh size or aspect ratio rather than directly on mesh size. In fact, even though the mesh used in this test case is also characterized by large variations in element size, a more gradual variation is present here and lower values of the aspect ratio are obtained.

Finally, we would like to note that the checkerboard-like pattern pointed out in the previous configurations for the NCF-indicator, has also been observed here over the course of the refinement process. This is however not noticeable in Fig. 10.

4.4. Periodic laminar flow past a cylinder at $Re = 100$

Finally, we investigate the applicability of the analysed refinement indicators to the simulation of unsteady flows. The considered test case is the unsteady periodic flow past a cylinder at $Re = 100$ and $M = 0.1$. The flow is two-dimensional, laminar, subsonic and unsteady periodic, characterized by the well known vortex shedding phenomenon.

The choice of a periodic flow allows for the comparison of different refinement indicators for the adaptive solution of an unsteady flow employing static p -refinement. The use of static p -refinement in place of a dynamic algorithm greatly simplifies the comparison. Indeed, for a dynamic p -refinement algorithm the choice of the marking strategy and the frequency of adaptation have a strong influence on the accuracy of the adaptive solution. In addition, a dynamic algorithm requires the use of a coarsening criterion which makes the comparison more complex.

4.4.1. Numerical details

The simulations are performed using a circular computational domain of radius $R = 200D$. The viscosity is assumed to be constant and adiabatic non-slip wall boundary conditions are applied on the cylinder wall. Far-field non-reflecting boundary conditions are applied at the outer boundary. An O-type 4th-order mesh is employed with 28 and 42 elements in the radial and azimuthal directions respectively. In the radial direction the element size varies following a geometric progression with ratio 1.2 up to $r = 4D$ and 1.24 up to the outer boundary.

The time discretization considered is a second-order Runge-Kutta Heun scheme with constant time step $\Delta t = 5 \cdot 10^{-3}$ normalised by the cylinder diameter and the reference velocity. We have verified that this choice does not have an influence on the solution.

A first simulation using a uniform polynomial degree $p = 2$ is performed until the flow is fully developed and a periodic state has been reached. For each successive uniform or adaptive refinement level, the simulations are performed by restarting from the previous solution. All simulations are let to evolve for at least 40 shedding cycles before extracting the quantities of interest. The refinement indicators are then computed and the p -adaptive algorithm is applied. The periodic state is considered to be reached when the variation in the Strouhal number and the average drag coefficient measured between two shedding cycles are respectively $\Delta St < 10^{-8}$ and $\Delta \overline{C_D} < 10^{-7}$.

The solution obtained from a simulation using a uniform polynomial degree $p = 7$ is used as a reference. The corresponding average drag coefficient $\overline{C_D}$, Strouhal number St and root mean square of the lift coefficient C'_L are reported in Table 2 and compared to the numerical and experimental results available in the literature.

For the p -adaptive algorithm, we consider the VMS, the spectral decay, the NCF and the normalized residual-based indicators. The residuum-NCF indicator is not included in this study. We have seen from the previous sections that this indicator provides a level of accuracy which is comparable to that provided by other estimators. However, as reported in Sec. 5 it requires a much higher computational cost for the current implementation in the Aghora solver.

In order to evaluate the time-independent refinement indicators used in the static p -refinement algorithm, 5 additional shedding cycles are simulated once the periodic state is achieved. The error estimators are computed at each subsequent time step. For each refinement indicator the element-wise maximum value in time is then used to define the time-independent error field as explained in Sec. 3.

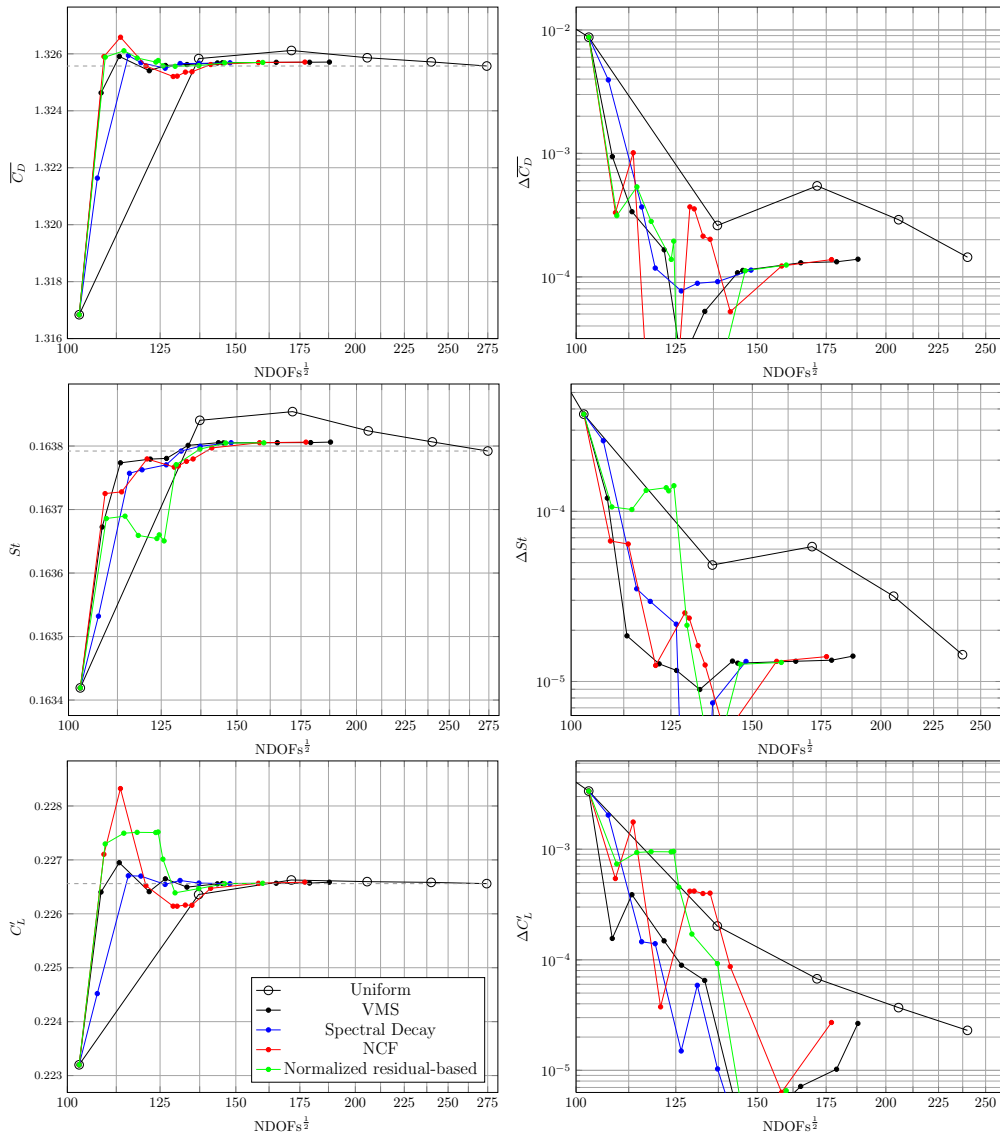


Figure 12: Laminar flow past a cylinder, $Re = 100$, $M = 0.1$: Convergence history of average drag coefficient, Strouhal number and rms of lift coefficient.

	$\overline{C_D}$	C'_L	St	M	domain size
Rajani et al. [50]	1.3353	0.1792	1.569	0	$R = 20D$
Ferrero et al. [51]	1.36	-	1.63	0.2	$R = 100D$
Posdziech et al. [49]	1.320	0.318	1.638	0	$h/2 = 200D$
Qu et al. [52]	1.319	0.225	1.648	0	$h/2 = 60D$
Tritton (exp) [53]	1.24 - 1.26	-	1.57 - 1.64		
Norberg (exp) [54]	-	0.227	1.64		
Wieselberg (exp) [55]	1.33	-	-		
Williamson (exp) [56]	1.33	-	1.60 - 1.64		
current	1.326	0.2266	1.638	0.1	$R = 200D$

Table 2: Flow parameters obtained through numerical simulations and experiments in the literature for the flow past a cylinder at $Re = 100$.

4.4.2. Analysis of the p -adaptive results

We start our comparison of different refinement indicators by analysing the convergence history of the global quantities $\overline{C_D}$, St and C'_L and their corresponding errors. These results are reported in Fig. 12. In this figure, we observe that all the refinement indicators are able to achieve the desired level of accuracy while reducing the number of DOFs by about 62% compared to uniform refinement.

It is interesting to note that, among the considered error estimation strategies, only the normalized residual-based indicator includes in its formulation a term related to the temporal evolution of the solution (see Eq. 21 and 27). For this reason, we would expect this refinement indicator to exhibit the best performance. However, this does not appear to be the case and similar if not superior results are produced by the other three refinement indicators. These results are in agreement with the conclusions drawn from the two N-S test cases previously considered.

In order to assess the performance of the normalized residual-based indicator, with respect to the VMS estimator, in resolving the near-wake region, for these two estimators the convergence history of the momentum density is analysed at two probes located respectively at $(x = 3D, y = 0D)$ on the symmetry plane and at $(x = 3D, y = 1D)$. The *rms* of the momentum density components at the first probe and the average momentum density components at the second are reported in Fig. 13. The two indicators actually lead to similar efficiency and a rapid convergence to the solution corresponding to a uniform polynomial degree $p = p_{\max} = 6$, as expected.

Following the same methodology employed for the previous test cases, we report in Fig. 14 and 15 the p -refinement level maps corresponding to $NDOFs^{\frac{1}{2}} \approx 145$. These results are in agreement with those obtained in the previously analysed configurations. The VMS and spectral decay indicators select the same refinement regions with higher refinement required by the latter in the low energy region at the base of the cylinder. The normalized residual-based indicator presents a smaller refinement region in the proximity of the cylinder. Moreover, we have observed that this indicator introduces higher levels of refinement in the near and far-wake region in the initial refinement steps. The NCF indicator shows a similar behaviour to the normalized residual-based indicator. The generation of the already described checkerboard-like pattern is also visible from the plots shown in Fig. 14c and 14d.

The results obtained for this configuration thus corroborate the conclusions drawn from the steady laminar test cases. These indicate that very similar performance can be obtained for the p -adaptive simulation of unsteady flows by employing the VMS and spectral decay indicators compared to the more complex and computationally expensive residual-based indicator.

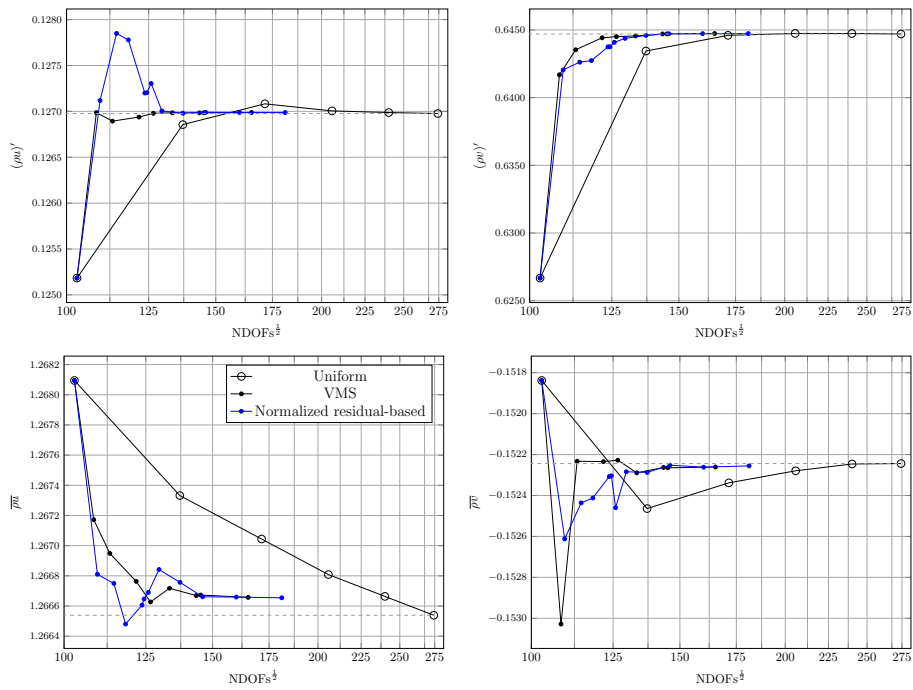


Figure 13: Laminar flow past a cylinder, $Re = 100$, $M = 0.1$: Convergence history of rms of momentum density components at location $[3D, 0D]$ (top) and average momentum density components at location $[3D, 1D]$ (bottom).

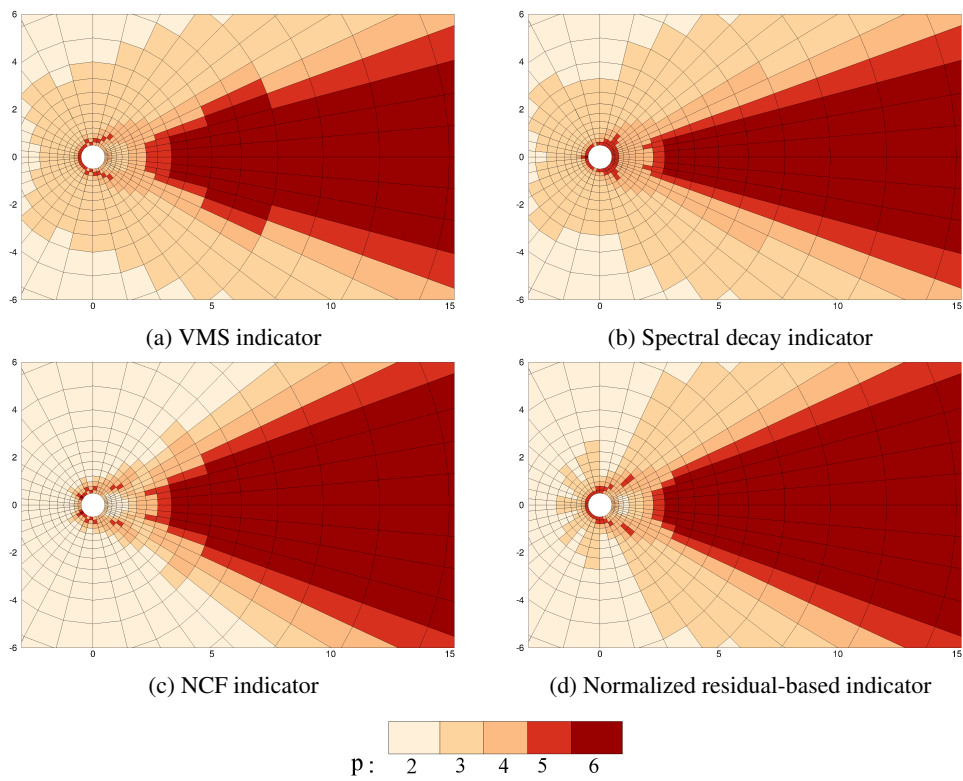


Figure 14: Laminar flow past a cylinder, $Re = 100$, $M = 0.1$: Local polynomial degree distribution obtained for different refinement indicators.

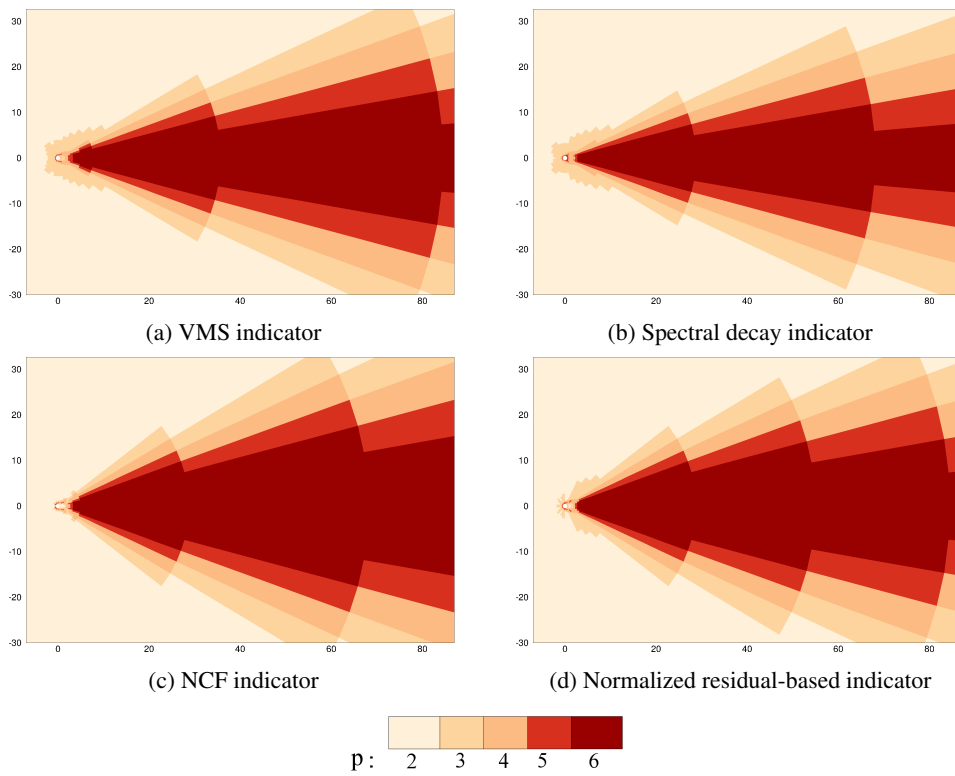


Figure 15: Laminar flow past a cylinder, $Re = 100$, $M = 0.1$: Local polynomial degree distribution obtained for different refinement indicators.

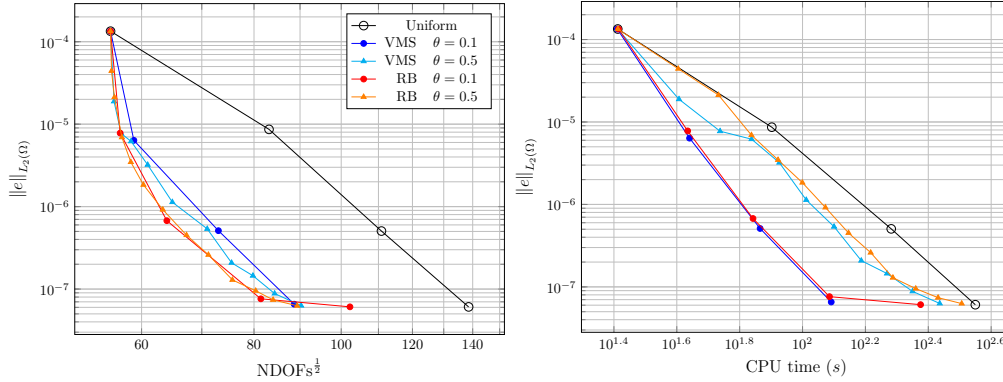


Figure 16: Euler flow over a Gaussian bump at $M = 0.5$: global entropy error vs number of DOFs and CPU time under uniform and adaptive refinement.

5. Implementation issues and computational cost

In section 4, the performance of the different refinement indicators has been analysed in terms of the reduction in the number of DOFs achieved by each estimator. It is indeed difficult to compare the computational time required by each approach due to the presence of several parameters that might affect the results and therefore the conclusions drawn.

To demonstrate the difficulties in carrying out such an analysis, we report in Fig. 16 the convergence history of the global entropy error for the inviscid flow over a Gaussian bump presented in section 4.1. The convergence history obtained using uniform p -refinement is also presented and compared to the results of adaptive p -refinement based on the VMS and residual-based indicators for two values of the marking fraction parameter: $\theta = 0.5$ and $\theta = 0.1$.

In the left panel of Fig. 16, the computational cost is expressed in terms of number of DOFs. Only minor differences can be identified when comparing the results obtained with the same indicator and the two values of θ . This illustrates that to a certain extent, the results obtained are not influenced by the specific marking procedure employed.

The right panel of Fig. 16 plots the error versus the computational cost in terms of CPU time for the same four simulations. Each simulation is restarted from the solution obtained at the previous refinement level and is performed on a single processor. It is clear that the choice of the marking fraction parameter or, more generally speaking, of the marking procedure, does have a strong influence on the number of refinement steps of the adaptive algorithm and consequently on the total computational time.

Another important aspect to take into account is that the computational cost of the refinement indicators depends significantly on the implementation details of the DG solver (e.g. modal or nodal approach). Finally, direct comparison in terms of computational times for distributed memory computations will also be influenced by the possibility of achieving a good load balance by taking into account the local polynomial degree p . These considerations indicate that comparing results in terms of CPU time would lead to conclusions that are specific to the CFD code, the numerical implementation, the marking algorithm and the test case considered.

In this section, we make some general observations that might be useful even when considering a different implementation from the one employed in our work. In particular, we consider

the locality properties of the refinement indicators and their possible effect on parallel efficiency, the ease of implementation in an existing CFD code and the number of operations required by each indicator.

As regards locality, we can see from the definition of the different refinement indicators provided in Sec. 3 that the only two indicators which are fully local are the VMS and spectral decay indicators as their computation only requires the knowledge of the solution inside the element (see. Eq. (13) and (15)). On the other hand, the computation of the NCF indicator (given in Eq. (17)) requires knowledge of the projection at the interface of the solution from the direct neighbours, while the residual-based and the residuum-NCF indicators will require additional information to be exchanged for the computation of the numerical fluxes. In the framework of distributed memory computations this lack of locality will involve blocking message passing operations which may lead to a reduced parallel efficiency.

Considering now the number of operations involved in the computation of each indicator, we observe that the VMS and spectral decay indicators require the projection of the solution on the reduced-order space S_h^{p-1} and the computation of the integrals required to evaluate the L_2 -norm in Eq. (13) and (15). In the case of a modal DG approach based on hierarchical basis functions, the scale separation is readily available and the required integrals can be efficiently computed by employing information contained in the mass matrix (see Tumolo et al. [2]). On the other hand, if a non-hierarchical basis is employed (e.g. nodal approach), the additional projection operation and the integration by quadrature necessary to compute the L_2 -norm will lead to higher computational cost. In this particular case, the NCF indicator would be more computationally efficient as it only requires the interpolation of the solution at the gauss points on each interface. As regards the residual-based and residuum-NCF indicators, their computation is more expensive as compared to the other indicators in either the nodal or modal approach. Indeed, the evaluation of the former requires the computation and integration over the elements and faces of the element residuals, numerical fluxes and the convective and diffusive fluxes obtained from the internal reconstruction $\mathcal{F}(\mathbf{u}_h^+, \nabla \mathbf{u}_h^+)$. Finally, we expect the residuum-NCF to be the most expensive among the considered indicators, regardless of the particular CFD solver considered. This is because, the contribution of the nonconformity error is more expensive to compute than the NCF indicator alone as it requires the integration of the jump terms that appear in the expression of the NCF indicator. The evaluation of the residuum-error contribution, on the other hand, requires the computation of the discrete residuals $\mathcal{N}_h(\mathbf{u}_h, \phi_i)$ with ϕ_i being the basis functions corresponding to the space S_h^{p+1} . To this we have to add the cost of the Lagrange multiplier method involved in the computation of this indicator which requires the solution of a linear system of size $(p_K + 2)^d$ for each element.

Finally, with regard to the ease of implementation, it is interesting to note that the complexity of computing the residuals corresponding to the refined polynomial space S_h^{p+1} , involved in the evaluation of the residuum-NCF indicator, strongly depends on the numerical implementation of the CFD method. In the case of a CFD code based on orthonormal basis functions built in the physical space, like the one employed in this work, this requires the computation and storage of the basis functions for S_h^{p+1} as well as their derivatives at the corresponding set of quadrature points. In general, important modifications of the employed CFD solver might be required to achieve a computationally efficient implementation of the residuum-NCF indicator. Similar considerations can be drawn for the residual-based indicator for which the different terms involved in its definition (Eq. (21) to (23)) depend directly on the set of equations being solved and the discretization employed. This is not the case for the VMS, spectral decay and NCF indicators which can be easily implemented even as external post-processing tools independently

of the employed solver.

6. Conclusion

In this work we have compared the performance of various refinement indicators for the p -adaptive simulation of steady and unsteady flows using DG methods. Five refinement indicators based on discretization-error and residual-error estimates have been considered. They have been selected for their potential suitability for the development of a dynamic p -adaptive algorithm for the simulation of unsteady turbulent flows. For this reason we have not considered in this study adjoint-based refinement indicators, due to their high computational cost in the context of unsteady flow simulations.

The considered indicators have been compared first in the context of three steady inviscid and viscous flow configurations: the inviscid flow over a Gaussian bump at $M = 0.5$, the laminar flow around a Joukowski airfoil at $\alpha = 0^\circ$, $M = 0.5$ and $\text{Re} = 1000$, and the laminar flow past a cylinder at $M = 0.1$ and $\text{Re} = 40$. The applicability of the obtained results for the simulation of unsteady flows has then been verified by considering static p -adaptive simulations of the flow past a cylinder at $M = 0.1$ and $\text{Re} = 100$.

The computational gain provided by a p -adaptive procedure based on any of the considered indicators has been clearly demonstrated. For all the configurations considered we have obtained a reduction in the number of degrees of freedom necessary to achieve the prescribed level of accuracy between 50% and 75% as compared to uniform p -refinement.

Overall, very similar results have been observed for all refinement indicators both in terms of convergence history and of the spatial regions selected for refinement. This is of interest because the VMS, spectral decay and NCF indicators require a very limited computational overhead and can be easily implemented as a post-processing operation. Moreover they do not depend on the physical model considered or the employed discretization. In contrast, the computation of the residual-based and residuum-NCF indicators might require a considerable effort in order to obtain an efficient implementation well-adapted for the solver at hand.

With regard to the VMS and spectral decay indicators, the former demonstrated similar if not superior performance as compared to the latter in each case considered. Moreover the VMS indicator presents a lower computational cost regardless of the employed implementation as the evaluation of the L_2 -norm used to normalize the spectral decay indicator does not need to be computed, as seen in Sec. 5.

On the other hand, the analysis of the distribution of polynomial degree yielded by the different refinement indicators, has revealed that the NCF, residual-based and residuum-NCF indicators present a stronger sensitivity to the mesh quality compared to the other indicators. Furthermore, the NCF indicator generates a checkerboard-like pattern which appears to be related to the refinement history and therefore the employed marking strategy. This pattern could potentially damage the convergence of the refinement algorithm and the accuracy of the solution as it introduces an irregularity in the spatial discretization. However, it is not excluded that this indicator could be used efficiently in conjunction with another refinement indicator, following for example an approach similar to the residuum-NCF indicator.

With all these considerations in mind, it can be argued that the VMS or spectral decay indicators constitute a good choice for p -adaptive simulations of unsteady flows, as they combine accuracy, computational efficiency and ease of implementation. The extension of these results to dynamic p -adaptive simulations of turbulent flows and hp -adaptation, in particular based on these two estimators, is the subject of current research.

Acknowledgments

This project has received funding from the European Union’s Horizon 2020 research and innovation programme under the Marie Skłodowska-Curie grant agreement No 675008. This work was performed using HPC resources from GENCI (Grant 2017-A0022A10129). We also thank Mathieu Lorteau, Emeric Martin, Florent Renac and Marie-Claire Le Pape for valuable discussions.

- [1] G. Kuru, M. de la Llave Plata, V. Couaillier, R. Abgrall, F. Coquel, An adaptive Variational Multiscale Discontinuous Galerkin Method for Large Eddy Simulation, in: 54th AIAA Aerospace Sciences Meeting, San Diego, California, AIAA, 2016.
URL <http://dx.doi.org/sci-hub/bz/10.2514/6.2016-0584>
- [2] G. Tumolo, L. Bonaventura, M. Restelli, A semi-implicit, semi-lagrangian, p-adaptive discontinuous galerkin method for the shallow water equations, *Journal of Computational Physics* 232 (1) (2013) 46–67.
URL <http://www.sciencedirect.com/science/article/pii/S0021999112003105>
- [3] P. Lesaint, P. A. Raviart, On a finite element method for solving the neutron transport equation, *Publications mathématiques et informatique de Rennes S4* (1974) 1–40.
URL <http://eudml.org/doc/273730>
- [4] W. H. Reed, T. R. Hill, Triangular mesh methods for the neutron transport equation, *Los Alamos Report LA-UR-73-479*.
- [5] B. Cockburn, C.-W. Shu, TVB Runge-Kutta local projection discontinuous Galerkin finite element method for conservation laws. II. General framework, *Mathematics of computation* 52 (186) (1989) 411–435.
- [6] B. Cockburn, C.-W. Shu, Runge–Kutta discontinuous Galerkin methods for convection-dominated problems, *Journal of scientific computing* 16 (3) (2001) 173–261.
- [7] J.-B. Chapelier, M. de la Llave Plata, F. Renac, E. Lamballais, Evaluation of a high-order discontinuous Galerkin method for the DNS of turbulent flows, *Computers & Fluids* 95 (2014) 210–226.
- [8] M. de la Llave Plata, V. Couaillier, M.-C. le Pape, On the use of a high-order discontinuous Galerkin method for DNS and LES of wall-bounded turbulence, *Computers & Fluids*.
- [9] C. J. Roy, Review of discretization error estimators in scientific computing, *AIAA Paper* 126 (2010) 2010.
- [10] P. Houston, E. Süli, A note on the design of hp-adaptive finite element methods for elliptic partial differential equations, *Computer Methods in Applied Mechanics and Engineering* 194 (2) (2005) 229–243.
- [11] W. F. Mitchell, M. A. McClain, A comparison of hp-adaptive strategies for elliptic partial differential equations, *ACM Transactions on Mathematical Software (TOMS)* 41 (1) (2014) 2.
- [12] S. M. Mitran, A comparison of adaptive mesh refinement approaches for Large-Eddy Simulation, Tech. rep., DTIC Document (2001).
- [13] J. Wackers, G. Deng, E. Guilmineau, A. Leroyer, P. Queutey, M. Visonneau, Combined refinement criteria for anisotropic grid refinement in free-surface flow simulation, *Computers & Fluids* 92 (2014) 209–222.
- [14] J. T. Oden, W. Wu, V. Legat, An hp adaptive strategy for finite element approximations of the Navier-Stokes equations, *International journal for numerical methods in fluids* 20 (8-9) (1995) 831–851.
- [15] V. Dolejší, P. Solin, hp-discontinuous Galerkin method based on local higher order reconstruction, *Applied Mathematics and Computation* 279 (2016) 219–235.
- [16] C. Mavriplis, Adaptive mesh strategies for the spectral element method, *Computer methods in applied mechanics and engineering* 116 (1) (1994) 77–86.
- [17] E. Creusé, S. Nicaise, A posteriori error estimator based on gradient recovery by averaging for convection–diffusion–reaction problems approximated by discontinuous Galerkin methods, *IMA Journal of Numerical Analysis* 33 (1) (2013) 212–241.
- [18] J. Banks, J. Hittinger, J. Connors, C. Woodward, Numerical error estimation for nonlinear hyperbolic PDEs via nonlinear error transport, *Computer Methods in Applied Mechanics and Engineering* 213 (2012) 1–15.
- [19] A. Syrakos, G. Efthimiou, J. G. Bartzis, A. Goulas, Numerical experiments on the efficiency of local grid refinement based on truncation error estimates, *Journal of Computational Physics* 231 (20) (2012) 6725–6753.
- [20] M. Kompenhans, G. Rubio, E. Ferrer, E. Valero, Adaptation strategies for high order discontinuous Galerkin methods based on tau-estimation, *Journal of Computational Physics* 306 (2016) 216–236.
- [21] R. Hartmann, P. Houston, Adaptive discontinuous Galerkin finite element methods for the compressible Euler equations, *Journal of Computational Physics* 183 (2) (2002) 508–532.
- [22] K. J. Fidkowski, D. L. Darmofal, Review of output-based error estimation and mesh adaptation in computational fluid dynamics, *AIAA journal* 49 (4) (2011) 673–694.
- [23] R. Hartmann, Multitarget error estimation and adaptivity in aerodynamic flow simulations, *SIAM Journal on Scientific Computing* 31 (1) (2008) 708–731.

- [24] D. Ekelschot, J. Peiró, S. Sherwin, Mesh adaptation strategies for compressible flows using a high-order spectral/hp element discretisation, Ph.D. thesis, Imperial College London (2016).
- [25] A. Abbà, L. Bonaventura, M. Nini, M. Restelli, Dynamic models for Large Eddy Simulation of compressible flows with a high order DG method, *Computers & Fluids* 122 (2015) 209–222.
URL <http://www.sciencedirect.com/science/article/pii/S0045793015002972>
- [26] O. Antepara, O. Lehmkuhl, R. Borrell, J. Chiva, A. Oliva, Parallel adaptive mesh refinement for Large-Eddy Simulations of turbulent flows, *Computers & Fluids* 110 (2015) 48–61.
- [27] M. Tugnoli, A. Abbà, L. Bonaventura, M. Restelli, A locally p-adaptive approach for Large Eddy Simulation of compressible flows in a DG framework, *Journal of Computational Physics* 349 (2017) 33–58.
URL <https://arxiv.org/abs/1610.03319>
- [28] F. Renac, M. de la Llave Plata, E. Martin, J.-B. Chapelier, V. Couaillier, Aghora: a high-order DG solver for turbulent flow simulations, in: *IDIHOM: Industrialization of High-Order Methods-A Top-Down Approach*, Springer, 2015, pp. 315–335.
- [29] L. Botti, Influence of reference-to-physical frame mappings on approximation properties of discontinuous piecewise polynomial spaces, *Journal of Scientific Computing* 52 (3) (2012) 675–703.
- [30] F. Bassi, S. Rebay, G. Mariotti, S. Pedinotti, M. Savini, A high-order accurate discontinuous finite element method for inviscid and viscous turbomachinery flows, in: *Proceedings of the 2nd European Conference on Turbomachinery Fluid Dynamics and Thermodynamics*, Antwerpen, Belgium, 1997, pp. 99–109.
- [31] F. Bassi, A. Crivellini, S. Rebay, M. Savini, Discontinuous Galerkin solution of the Reynolds-averaged Navier-Stokes and $k-\omega$ turbulence model equations, *Computers & Fluids* 34 (4) (2005) 507–540.
- [32] T. J. Hughes, L. Mazzei, K. E. Jansen, Large eddy simulation and the variational multiscale method, *Computing and visualization in science* 3 (1) (2000) 47–59.
- [33] C. Mavriplis, A posteriori error estimators for adaptive spectral element techniques, in: *Proceedings of the Eighth GAMM-Conference on Numerical Methods in Fluid Mechanics*, Springer, 1990, pp. 333–342.
- [34] C. Mavriplis, Nonconforming discretizations and a posteriori error estimators for adaptive spectral element techniques, Ph.D. thesis, Massachusetts Institute of Technology (1989).
- [35] P.-O. Persson, J. Peraire, Sub-cell shock capturing for discontinuous galerkin methods, in: *44th AIAA Aerospace Sciences Meeting and Exhibit*, 2006, p. 112.
- [36] G. Gassner, C. Altmann, F. Hindenlang, M. Staudenmeier, C. Munz, Explicit discontinuous Galerkin schemes with adaptation in space and time, 36th CFD/ADIGMA course on hp-adaptive and hp-multigrid methods, VKI LS.
- [37] G. Tumolo, L. Bonaventura, A semi-implicit, semi-lagrangian discontinuous galerkin framework for adaptive numerical weather prediction, *Quarterly Journal of the Royal Meteorological Society* 141 (692) (2015) 2582–2601.
URL <http://onlinelibrary.wiley.com/doi/10.1002/qj.2544/full>
- [38] L. Krivodonova, J. E. Flaherty, Error estimation for discontinuous galerkin solutions of two-dimensional hyperbolic problems, *Advances in Computational Mathematics* 19 (1-3) (2003) 57–71.
- [39] L. Krivodonova, J. Xin, J.-F. Remacle, N. Chevaugnon, J. E. Flaherty, Shock detection and limiting with discontinuous galerkin methods for hyperbolic conservation laws, *Applied Numerical Mathematics* 48 (3-4) (2004) 323–338.
- [40] M. Ainsworth, A posteriori error estimation for Discontinuous Galerkin finite element approximation, *SIAM Journal on Numerical Analysis* 45 (4) (2007) 1777–1798.
- [41] R. Hartmann, J. Held, T. Leicht, F. Prill, Error estimation and adaptive mesh refinement for aerodynamic flows, in: *ADIGMA-A European Initiative on the Development of Adaptive Higher-Order Variational Methods for Aerospace Applications*, Springer, 2010, pp. 339–353.
- [42] V. Dolejší, hp-DGFEM for nonlinear convection-diffusion problems, *Mathematics and Computers in Simulation* 87 (2013) 87–118.
- [43] V. Dolejší, F. Roskovec, M. Vlasák, Residual based error estimates for the space-time discontinuous Galerkin method applied to the compressible flows, *Computers & Fluids* 117 (2015) 304–324.
- [44] V. Dolejší, A design of residual error estimates for a high order BDF-DGFE method applied to compressible flows, *International Journal for Numerical Methods in Fluids* 73 (6) (2013) 523–559.
- [45] Z. J. Wang, K. Fidkowski, R. Abgrall, F. Bassi, D. Caraeni, A. Cary, H. Deconinck, R. Hartmann, K. Hillewaert, H. T. Huynh, et al., High-order CFD methods: current status and perspective, *International Journal for Numerical Methods in Fluids* 72 (8) (2013) 811–845.
- [46] 4th International Workshop on High-Order CFD Methods (June 2016).
URL <https://how4.cenaero.be/content/participants>
- [47] 5th International Workshop on High Order CFD Methods (January 2018).
URL <https://how5.cenaero.be/>
- [48] R. Gautier, D. Biau, E. Lamballais, A reference solution of the flow over a circular cylinder at $Re=40$, *Computers & Fluids* 75 (2013) 103–111.
- [49] O. Posdziech, R. Grundmann, A systematic approach to the numerical calculation of fundamental quantities of the

- two-dimensional flow over a circular cylinder, *Journal of Fluids and Structures* 23 (3) (2007) 479–499.
- [50] B. Rajani, A. Kandasamy, S. Majumdar, Numerical simulation of laminar flow past a circular cylinder, *Applied Mathematical Modelling* 33 (3) (2009) 1228–1247.
- [51] A. Ferrero, F. Larocca, G. Puppo, A robust and adaptive recovery-based discontinuous galerkin method for the numerical solution of convection–diffusion equations, *International Journal for Numerical Methods in Fluids* 77 (2) (2015) 63–91.
- [52] L. Qu, C. Norberg, L. Davidson, S.-H. Peng, F. Wang, Quantitative numerical analysis of flow past a circular cylinder at reynolds number between 50 and 200, *Journal of Fluids and Structures* 39 (2013) 347–370.
- [53] D. Tritton, Experiments on the flow past a circular cylinder at low reynolds numbers, *Journal of Fluid Mechanics* 6 (4) (1959) 547–567.
- [54] C. Norberg, An experimental investigation of the flow around a circular cylinder: influence of aspect ratio, *Journal of Fluid Mechanics* 258 (1994) 287–316.
- [55] C. v. Wieselsberger, Neuere feststellungen uber die gesetze des flussigkeits und luftwiderstands, *Phys. Z.* 22 (1921) 321.
- [56] C. Williamson, Oblique and parallel modes of vortex shedding in the wake of a circular cylinder at low reynolds numbers, *Journal of Fluid Mechanics* 206 (1989) 579–627.